# Aperture Synthesis Observations of the Nearby Spiral NGC 6503: Modeling the Thin and Thick HI Disks

Eric W. Greisen[1], Kristine Spekkens[23],
and
Gustaaf A. van Moorsel[1]

## ABSTRACT

We present sensitive aperture synthesis observations of the nearby, late-type spiral galaxy NGC 6503, and produce HI maps of considerably higher quality than previous observations by van Moorsel & Wells (1985). We find that the velocity field, while remarkably regular, contains clear evidence for irregularities. The HI is distributed over an area much larger than the optical image of the galaxy, with spiral features in the outer parts and localized holes within the HI distribution. The absence of absorption towards the nearby quasar 1748+700 yields an upper limit of $5 \times 10^{17}\,\mathrm{cm}^{-2}$ for the column density of cold HI gas along a line of sight which should intersect the disk at a radius of 29 kpc. This suggests that the radial extent of the HI disk is not much larger than that which we trace in HI emission (23 kpc). The observed HI distribution is inconsistent with models of a single thin or thick disk. Instead, the data require a model containing a thin disk plus a thicker low column-density HI layer that rotates more slowly than the thin disk and that extends only to approximately the optical radius. This suggests that the presence of extra-planar gas in this galaxy is largely the result of star formation in the disk rather than cold gas accretion. Improved techniques for interferometric imaging including multi-scale Clean that were used in this work are also described.

*Subject headings:* galaxies: individual (NGC 6503) — galaxies: ISM — galaxies: kinematics and dynamics — galaxies: spiral — methods: data analysis

## 1. Introduction

Attention was drawn to the relatively nearby, low-luminosity spiral galaxy NGC 6503 by the occurrence of a bright quasar only 5.3 arc minutes away. Deep optical plates taken by Arp et al. (1976) show wisps or spiral arms in the outermost portions of the NW part of the galaxy, which were in the direction of, but did not approach, the quasar. The neutral hydrogen was observed with the Westerbork Synthesis Radio Telescope by Shostak, Willis, & Crane (1981) and later with the early, incomplete VLA by van Moorsel & Wells (1985). Neither group found any connection between the quasar and the galaxy. The images obtained by van Moorsel & Wells (1985) revealed a very regular rotation curve, but were sensitive only down to a column density of $1.3 \times 10^{20}$ cm$^{-2}$.

Although quasars are no longer thought to be directly linked to nearby galaxies, NGC 6503 remains an interesting target: its proximity, isolation, and regular kinematics make it ideal for detailed structural studies to understand better the formation and evolution of nearby spirals. We therefore undertook to re-observe this galaxy using the full VLA with improved receivers in the C array in order to obtain substantially better spatial and spectral resolution with improved sensitivity. Improvements in software allowed us to take advantage of the bright quasar for calibration with-

[1]National Radio Astronomy Observatory, P.O. Box O, Socorro, NM 87801, U.S.A.

[2]Department of Physics, Royal Military College of Canada, P.O. Box 17000, Stn Forces, Kingston ON, K7K 7B4

[3]Previously a Jansky Fellow of the National Radio Astronomy Observatory.

out suffering the sidelobe problems encountered particularly by Shostak, Willis, & Crane (1981) and further improvements allowed us to image the galaxy with very little loss of fidelity due to missing short spacings.

Deep HI observations of nearby spirals have revealed a wealth of low column density features at anomalous positions and velocities. In particular, studies of systems such as NGC 2403 (Schaap, Sancisi, & Swaters 2000; Fraternali et al. 2002), NGC 2613 (Chaves & Irwin 2001), NGC 4559 (Barbieri et al. 2005), NGC 891 (Oosterloo, Fraternali, & Sancisi 2007), UGC 7321 (Matthews & Wood 2003), NGC 253 (Boomsma et al. 2005), NGC 6946 (Boomsma et al. 2008) and M83 (Miller et al. 2008) suggest that extra-planar gas with decreasing rotation velocity with increasing height from the disk may be ubiquitous in these systems (see Fraternali (2008) for a complete list). This anomalous gas is not clearly associated with previous interactions or the presence of companions. It has been proposed that this extra-planar HI stems from a galactic fountain mechanism produced by feedback from supernovae in the disk (e.g Collins et al. 2002; Fraternali & Binney 2006; Oosterloo, Fraternali, & Sancisi 2007; Boomsma et al. 2008; Miller et al. 2008), although at least some of it must stem from cold gas accretion from the intergalactic medium (e.g. Barnabè et al. 2006; Kaufmann et al. 2006; Fraternali & Binney 2008; Sancisi et al. 2008). It has proven difficult to distinguish between these two possibilities, however, in part because many of the galaxies imaged in HI are actively forming stars.

NGC 6503 is an interesting system to examine in this context because it offers the possibility of distinguishing between the star formation and gas accretion hypotheses. It has a relatively modest star formation rate and an HI layer that extends far beyond the star-forming disk. If primordial gas accretion is a dominant contributor to the extra-planar HI, one would expect little correlation between this layer and the star-forming disk. On the other hand, if star formation were responsible, one wouldn't expect to find a thick HI layer beyond the optical disk.

The data set presented in this paper provides sensitive HI maps of NGC 6503. Dynamical models of this galaxy obtained from these data in combination with high-quality H$\alpha$ and CO kinematics are forthcoming. Here, we describe our HI observations and the derived properties of NGC 6503 in preparation for that work, and model the properties of its extra-planar HI. In the appendix, we introduce improved image deconvolution algorithms, describing in some detail the particular implementation, widely available in the astronomical community, used on the present data.

### 1.1. Known properties of NGC 6503

The basic properties of NGC 6503 are summarized in Table 1. The galaxy is a late-type, low luminosity spiral located near the Local Void (Karachentsev et al. 2003). Deep optical surveys have not found any galaxies near NGC 6503, making it a very isolated, probably unperturbed system. We note that because of its large angular size, it is not included in standard isolated galaxy catalogs (e.g. Verdes-Montenegro et al. 2005).

Due to its proximity, the distance to NGC 6503 cannot be determined reliably from its recessional velocity. Photometry of the brightest stars in the galaxy led Karachentsev & Sharina (1997) (see also Karachentsev et al. (2003)) to derive its distance as 5.2 Mpc, a value that we adopt in this study. The Hubble type of SA(s)cd from de Vaucouleurs et al. (1991) indicates that NGC 6503 has an S shape and no bar, but Lira et al. (2007) prefer a Hubble type of Sc rather than Scd. Makarova (1999) presents B, V, and I surface brightness profiles traced to 200 arcsec radius, and finds the radius of NGC 6503 at 25$^{\rm th}$ magnitude per square arcsec to be 116.6, 140.6, and 198.9 arcsec, respectively at these bands. The central surface brightness of NGC 6503 lies in the range found for normal disk galaxies.

We compute the global star formation rate of NGC 6503 using the Kennicutt (1998) IR star formation relation using the measurements of Sanders et al. (2003), following the method outlined by Kewley et al. (2002). Its modest star formation rate explains its low B-band luminosity compared to normal spirals of the same morphological type, even when this quantity is normalized by the galaxy size and/or mass (Roberts & Haynes 1994).

NGC 6503 is in general a fairly normal, if rather modest, low-luminosity galaxy with very regular kinematics. However, in the center of this galaxy,

Table 1: NGC 6503 properties

| parameter | value | reference |
|---|---|---|
| Right ascension (J2000) | $17^{h}49^{m}26^{s}.30$ | this work |
| Declination (J2000) | $70°08'40.7''$ | this work |
| Systemic Velocity (heliocentric) | $28.2 \pm 0.3$ km s$^{-1}$ | this work |
| Distance | 5.2 Mpc | Karachentsev & Sharina (1997) |
| optical radius (25$^{th}$ B mag/ss) | $3.55'$ | de Vaucouleurs et al. (1991) |
| optical radius | 5.35 kpc | at 5.2 Mpc |
| Hubble type | SA(s)cd | de Vaucouleurs et al. (1991) |
| Absolute B magnitude | -17.68 | Makarova (1999) |
| B luminosity | $1.5 \times 10^{9}$ L$_{\odot}$ | |
| B central surface brightness | 20.05 mag arcsec$^{-2}$ | Makarova (1999) |
| Star formation rate | $0.18\,M_{\odot}\,yr^{-1}$ | this work |

Lira et al. (2007) find a bright central nucleus which exhibits "prominent LINER emission lines and a red continuum with strong absorption features." Additionally, they find six point sources of X-ray emission. Ho, Filippenko, Sargent (1997) call the nucleus a "transition" or even Seyfert type 2 with some uncertainty. The presence of some continuum radio emission in a larger, but central region of NGC 6503 (Section 3.1), suggests that this galaxy hosts a low-luminosity active galactic nucleus (AGN).

## 2. Observations and reductions

NGC 6503 was observed on 27 February 1996 with the VLA in C configuration. There were 127 spectral channels separated by 24.4 kHz (5.15 km s$^{-1}$) centered on 26 km s$^{-1}$ heliocentric radial velocity. The sources used for bandpass shape and absolute flux density calibration were 3C286 and 3C48, and were observed at the beginning, middle, and end of the session for a total of about 43 minutes. The total integration time on NGC 6503 was a little more than 500 minutes, interspersed every 50 minutes or less with 2-minute observations of the 2.0-Jy amplitude and phase calibrator 1800+784. The observing setup is summarized in Table 2.

All data reduction was done in the AIPS software package (Greisen 2003). After deleting $\sim 2\%$ of the data for various reasons such as scan start-up problems and spurious amplitudes and phases, the amplitude and phase calibrations were applied to NGC 6503 (and 1800+784). The bandpass shapes were determined from the 3C286 and 3C48 observations, interpolated in time, and applied to NGC 6503 and 1800+784. Five channels exhibiting weak Galactic HI absorption were flagged in 3C48, and the bandpass was interpolated across them before being applied to the data.

The 0.76-Jy quasar 1748+700, in the same beam as NGC 6503, dominates the data in all continuum channels. To separate the continuum and line signals, the data for NGC 6503 were phase shifted to the quasar position and straight lines (with slope) were fit to the spectrum of the real and imaginary parts of each visibility sample using a total of 50 channels from the band edges which were judged to be both free of line signal and bandpass edge effects. A line-only dataset was produced by subtracting the fits from the visibility data and shifting back to the original phase center, while the best-fitting continuum values at the band center were adopted as the continuum-only dataset. A task similar to the one used is described by Cornwell, Uson, & Haddad (1992).

All imaging and deconvolution were done with the AIPS program IMAGR using a tempered uniform weighting ("robust weighting", Briggs et al. (1999)). The point-source response was nearly circular. We used IMAGR's multi-scale Clean algorithm to deconvolve the synthesized beam from both the continuum and line datasets. Because this functionality has not yet been thoroughly described in the literature, we discuss it in detail in Appendix A. The final image properties are summarized in Table 2.

The continuum was imaged over an area approximately 2.5° in diameter in order to cover both the primary beam and the first outer sidelobe of the individual VLA antennas. A few more distant regions surrounding nearby NVSS sources (Condon et al. 1998) were also included. The area was imaged in 55 facets (Cornwell & Perley 1992) in order to avoid wide-field distortions. The deconvolution was performed with a multi-scale Clean using Gaussian model sources with full-width half-maximum (FWHM) sizes of 0″, 36″, and 108″, and Cleaning was stopped when the peak residual in each facet fell below a flux density cutoff of 0.21, 0.42, and 1.7 mJy/beam, respectively. The "bias" parameter controlling the facet Cleaning order was $b = 0.62$ (see Appendix A).

The proximity to NGC 6503 of the bright quasar 1748+700, as well as other continuum sources, allows for an accurate self-calibration to improve the amplitude and phase calibration, as initially described by Schwab (1980). The implementation in AIPS uses the full multi-scale, multi-facet Clean model to compute model visibilities which are divided into observed visibilities to get apparent baseline-dependent gains. A least-squares method turns these into antenna-dependent gains which are applied to the observations before another round of imaging. Given the quality of the initial calibration using 1800+784 and the strength of 1748+700, the self-calibration iterations converged quite rapidly. After imaging, deconvolution and several rounds of self-calibration, the 55 separate facet images were interpolated onto a "flattened" image with no loss of intensity or positional accuracy. The final continuum image has a resolution of 14″, a root mean square (RMS) of 80 $\mu$Jy/beam and a dynamic range in excess of 9000:1.

The improved amplitude and phase solutions from the self-calibration and some additional editing were then applied to the HI visibility data. Each channel was imaged in a single $50' \times 50'$ facet. The deconvolution was performed with a multi-scale Clean using Gaussian model sources with FWHMs of 0″, 36″, 108″ and 324″, flux density cutoffs of 0.2, 0.55, 2.6, and 7.8 mJy/beam respectively, and a bias parameter $b = 0.62$ (see Appendix A). The Clean was limited interactively to the regions which clearly had emission in that channel in order to mitigate the well-known Clean bias (Condon et al. 1998). The final HI data cube has an RMS noise of 0.58 mJy/beam, a spatial resolution of 14″ per channel, and a peak dynamic range of 30:1.

## 3. Images

The properties of the full-resolution continuum and HI images of NGC 6503 are summarized in Table 2. Below, we discuss each in turn.

### 3.1. Continuum in NGC 6503 and in 1748+700

The total Cleaned flux density from the 2.5° diameter continuum image in the vicinity of NGC 6503 is 967 mJy, uncorrected for attenuation from the primary beam of the individual VLA antennas. There are $\sim$ 90 sources with a signal-to-noise ratio $S/N > 5$ in the image, some of which are in the first and second outer sidelobes of the primary beam. The sources are essentially all unresolved except for NGC 6503.

Fig. 1 presents a portion of the primary beam-corrected image of the continuum emission in the vicinity of NGC 6503. As expected, the noise in the image rises rapidly towards the edge of the primary beam. The total image size is governed by the beam correction itself, since the VLA's primary beam is completely unknown beyond 30′ at this frequency. The paucity of continuum sources near NGC 6503 and 1748+700 as well as the apparent chain of sources east of the pair is initially striking, but not statistically significant (J. J. Condon, priv. comm.). The extent of the HI emission in NGC 6503 (see Section 4.1) is represented by the solid line in Fig. 1. Qualitatively, the centroids and position angle of the HI and continuum emission are in good agreement, with the HI extending well beyond the continuum.

The continuum properties of NGC 6503 are summarized in Table 3. The primary-beam corrected total flux density of the extended continuum source in NGC 6503 is 39 $\pm$ 1.2 mJy. A contour image of the continuum radio source in NGC 6503 is shown in Fig. 2. The position angle is close to the -60 degrees found in the HI. The full extent along the major axis is about 200″or 5 kpc at the adopted distance. The continuum appears to peak at the three locations marked by crosses. The HI is at a minimum in the cen-

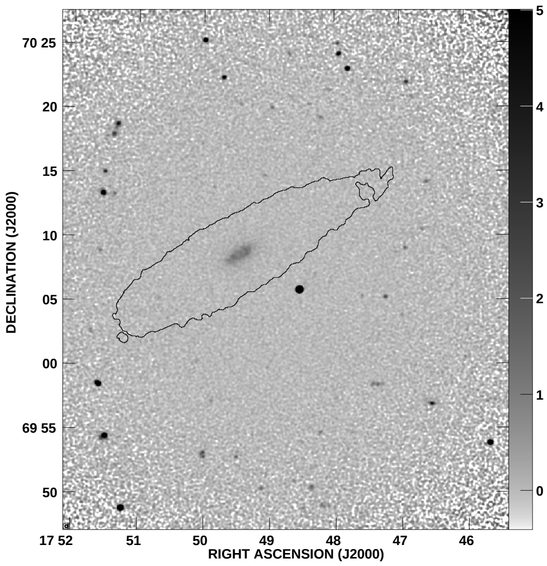


Fig. 1.— Primary beam-corrected continuum image of a field near NGC 6503. The wedge to the right shows the displayed brightness in mJy/beam which is clipped at 5 mJy/beam. The extent of the detected HI emission is shown by the solid line (see Section 4.1). The quasar 1748+700 is the strong point source 5.34′ to the SW of the galaxy.

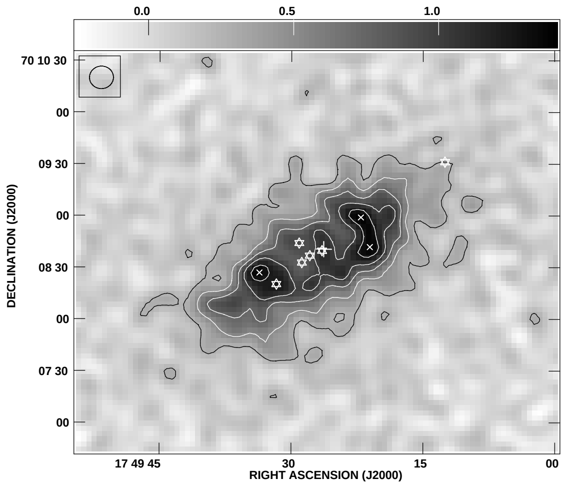


Fig. 2.— 21-cm radio continuum distribution in NGC 6503. The wedge at the top shows the displayed brightness in mJy/beam, and the contours are drawn at (1, 2, 3, 4, 5) × 0.25 mJy/beam. The Clean beam is plotted in the top left corner. The continuum peaks are marked by crosses, the 6 unresolved X-ray sources found by Lira et al. (2007) are marked by stars, and the kinematic center of the HI distribution (Section 4.2) is marked by a plus sign.

Table 2: Observing setup and image properties

| parameter | value | units |
|---|---|---|
| VLA array configuration | C | |
| Primary beam FWHM | 29.7 | arc minutes |
| Time on-source | 500 | min. |
| Usable total bandwidth | 2513 | kHz |
| Band center (heliocentric) | 26 | km s$^{-1}$ |
| Spatial resolution | 14 | arcsec |
| Spatial resolution | 0.35 | kpc |
| Effective cont. bandwidth | 1220 | kHz |
| RMS image noise (cont.) | 0.08 | mJy/beam |
| Dynamic range (cont.) | 9000 | |
| Channel separation (line) | 5.15 | km s$^{-1}$ |
| RMS image noise (line) | 0.58 | mJy/beam |
| Peak dynamic range (line) | 30 | |

ter, but has peaks near the other three locations. The apparent ridge in the continuum in the NW crosses a region in which the HI is minimal, suggesting that this correspondence is probably not causal. The six unresolved X-ray sources found by Lira et al. (2007) are also illustrated with stars. That the central continuum radio peak is coincident with an X-ray source is further evidence for a low-luminosity AGN (Ho, Filippenko, Sargent 1997).

With primary beam correction, the total flux density of the quasar 1748+700 was 755 mJy on the observation date. Within reasonable uncertainties the quasar is unresolved.

### 3.2. HI in NGC 6503

Fig. 3 shows the detected HI emission from NGC 6503 in a selection of channels. It is clear that even at the higher resolution and sensitivity of our data relative to those of van Moorsel & Wells (1985), the HI kinematics of NGC 6503 are remarkably regular. Nonetheless, when the channel images are examined in detail, irregularities are apparent. The outer portions of many emission "wings" bend away from the major axis, most noticeably at -25.5 km s$^{-1}$, -10.1 km s$^{-1}$ and 82.7 km s$^{-1}$ in Fig. 3. There are also spatially distinct features in the distribution of some channels, such as at -25.5 km s$^{-1}$ and 98.2 km s$^{-1}$. We investigate the HI morphology and kinematics of NGC 6503 in detail in Section 4.

Fig. 4 shows selections from the data cube after rotation and transposition, plotting the HI as a function of velocity and position along lines parallel to the major axis. The central panel is the traditional rotation curve image of this galaxy. Fig. 5 shows position-velocity images along the minor axis at several positions on the major axis. These figures are made from the full resolution image using a single 3-arcsecond pixel on the third axis for each panel with no additional smoothing. At first glance, the position-velocity slices of NGC 6503 exhibit considerable symmetry and do not appear to show an extensive "beard" of HI emission at velocities between the rotation velocity and the systemic velocity, as found for several other systems (Fraternali et al. 2002; Matthews & Wood 2003; Boomsma et al. 2005; Oosterloo, Fraternali, & Sancisi 2007). In Section 4.4, we place quantitative constraints on the morphology and kinematics of the extra-planar HI layer that is consistent with the present data. The bottom panel in Fig. 5 in particular shows some significant asymmetry. This is associated with the warp to the SW discussed further in Section 4.3 in connection with Fig. 13.

### 3.3. HI in the vicinity of NGC 6503

We searched the data cube outside the confines of NGC 6503 for any other source of line emission. Due to limitations of the VLA correlator and the dishes that make up the array, a bandwidth of only about 500 km s$^{-1}$ was observed, centered at 26 km s$^{-1}$ heliocentric, over a region about 50′in diameter. No other extragalactic HI emission was found. For an unresolved source spanning two contiguous velocity channels at the distance of NGC 6503, this non-detection corresponds to a $3\sigma$ HI mass limit that varies between $M_{HI} = 1.1 \times 10^5\, M_\odot$ at the pointing center and ten times this value near the edge of the field. In the limited volume probed by our observations, NGC 6503 appears isolated from an HI standpoint as well as from an optical one.

### 3.4. Absorption towards 1800+784 and 1748+700

The calibration source 1800+784 is located at Galactic longitude $l = 110.0°$, latitude $b = 29.1°$, while NGC 6503 is at $l = 100.5°$, $b = 30.7°$. These directions are expected to have local Milky Way HI emission and, most likely, absorption. Indeed, Fig. 6 shows an absorption line in the spectrum of 1800+784, with a depth of 0.040 ± 0.002 Jy or an optical depth of 0.02. The line is centered at an LSR velocity of -1.6 km s$^{-1}$ with a FWHM of 13 km s$^{-1}$.

By contrast, Fig. 7 shows that no absorption is observed in the direction of the quasar 1748+700 ($l = 100.5°$, $b = 30.8°$) to very high precision. The deepest negatives in the full resolution image in this direction (light line) are less than 1 mJy/beam, while the spectrum extracted from an image smoothed to 30″ and 10 km s$^{-1}$ resolution (heavy line) shows even less evidence for absorption. The optical depth toward 1748+700 is thus, conservatively, $\tau = 0.0 \pm 0.001$. This suggests that, for HI of line width 5 km s$^{-1}$ and temperature 50 K, the column density upper limit is $5 \times 10^{17}$cm$^{-2}$. Assuming a thin, flat disk in NGC 6503, the line

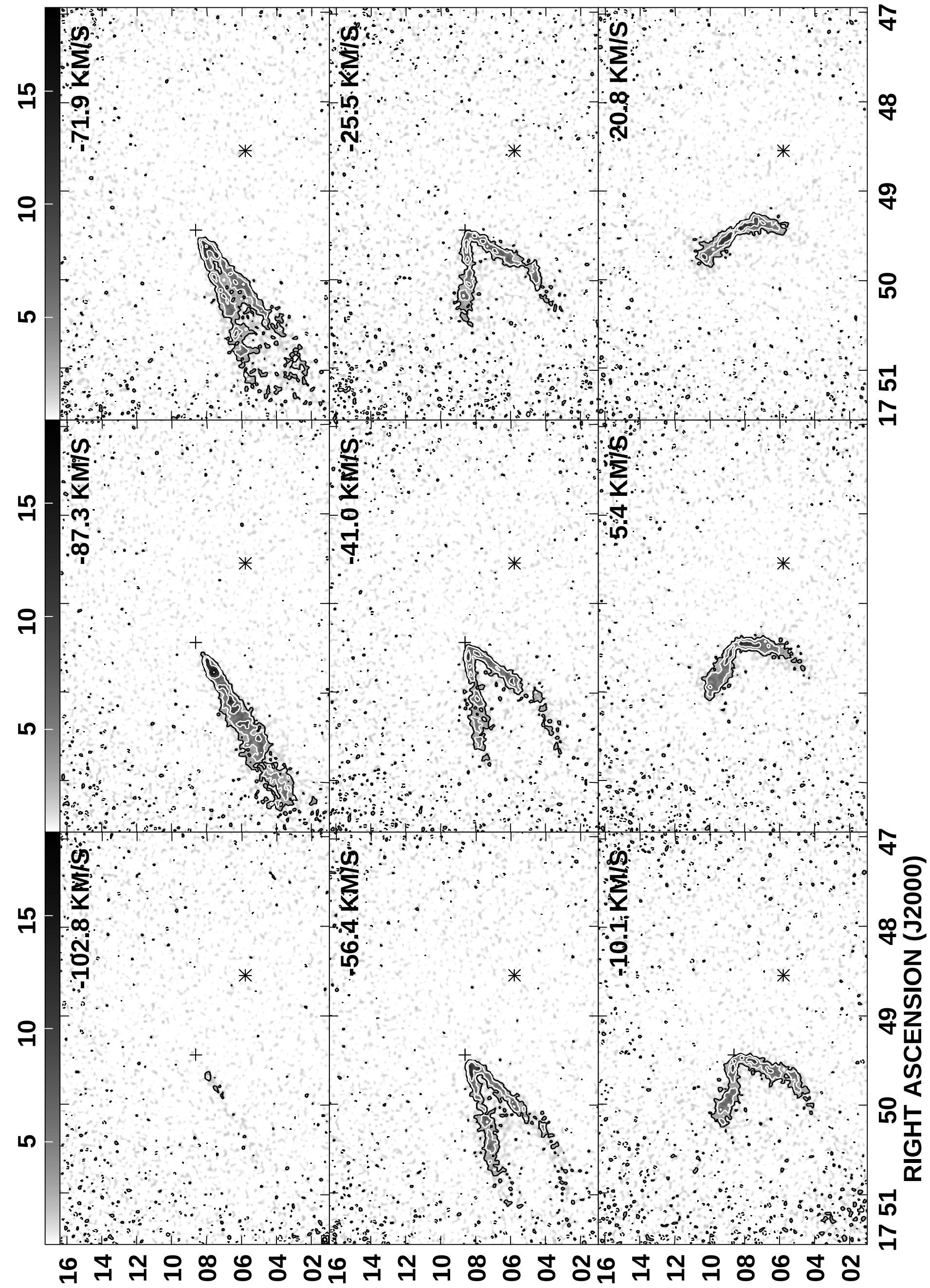


Fig. 3.— Primary-beam corrected channel images of the HI emission in NGC 6503. The gray-scale is plotted from 0.5 to 18.65 mJy/beam with a logarithmic transfer function and contours are plotted at -2, 2, 4, 8, and 16 mJy/beam. (The negative contours appear only in regions which are noise dominated.) The heliocentric radial velocity of the channel is in the upper right corner, and the Clean beam is plotted in the lower left corner of the first panel. The kinematic center of NGC 6503 is marked with a plus sign and the quasar 1748+700 is marked with an asterisk.

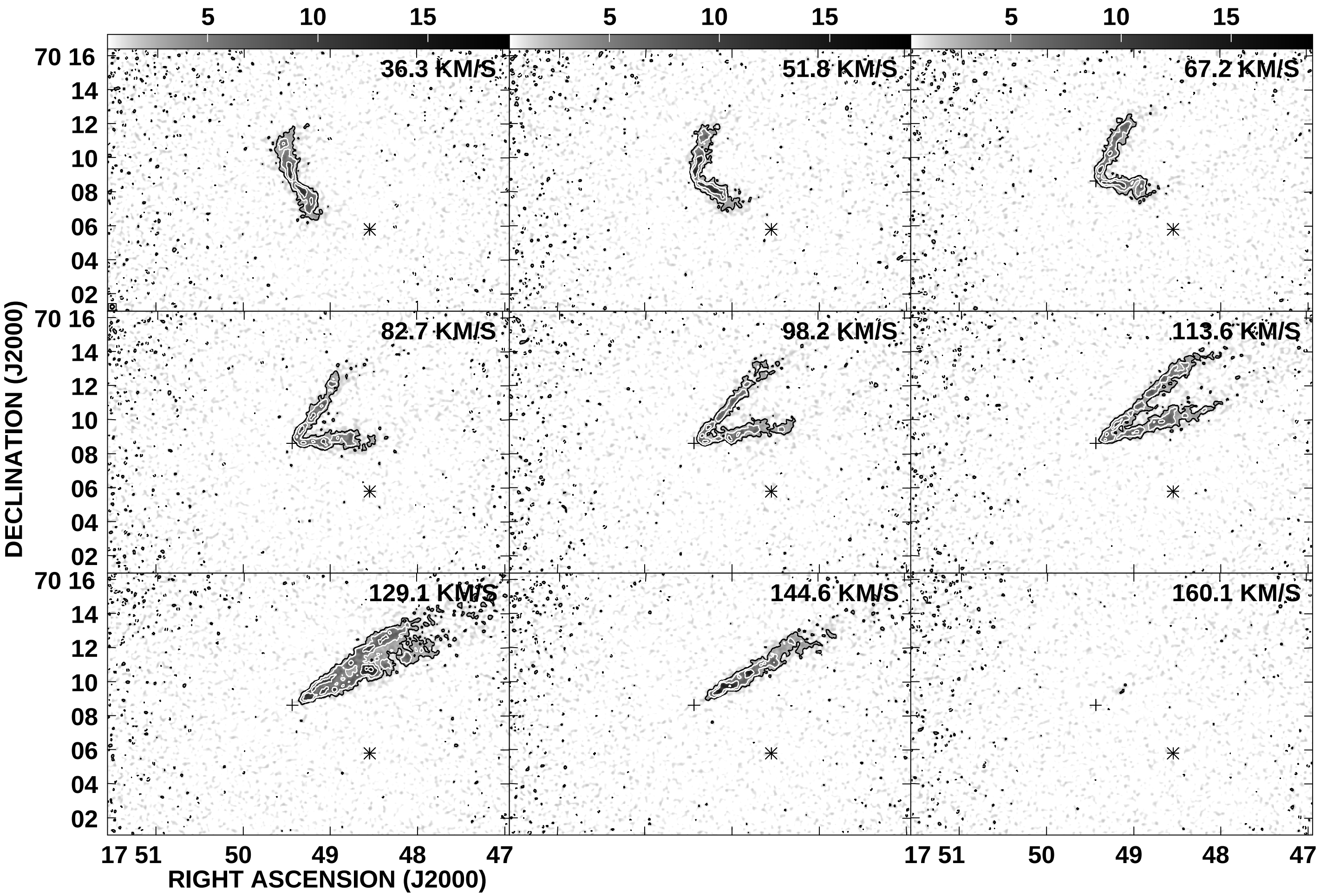


Fig. 3.— *Continued.*

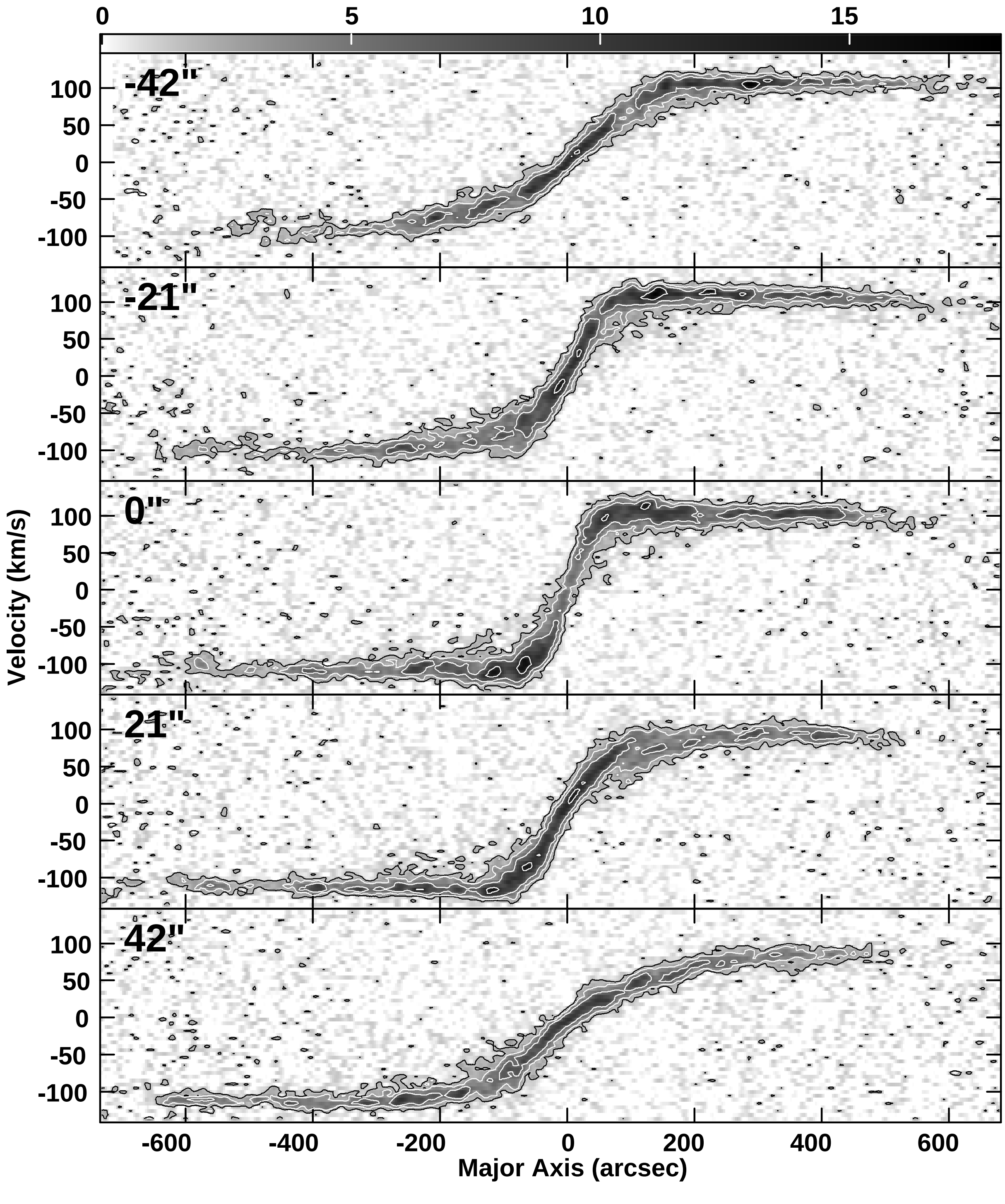


Fig. 4.— Primary-beam corrected images for slices parallel to the major axis, separated by 21″. Axis labels are relative to the kinematic center and the systemic velocity. The gray-scale is plotted from 0.5 to 18.65 mJy/beam with a logarithmic transfer function and contours are plotted at 1.5, 3, 6, and 12 mJy/beam.

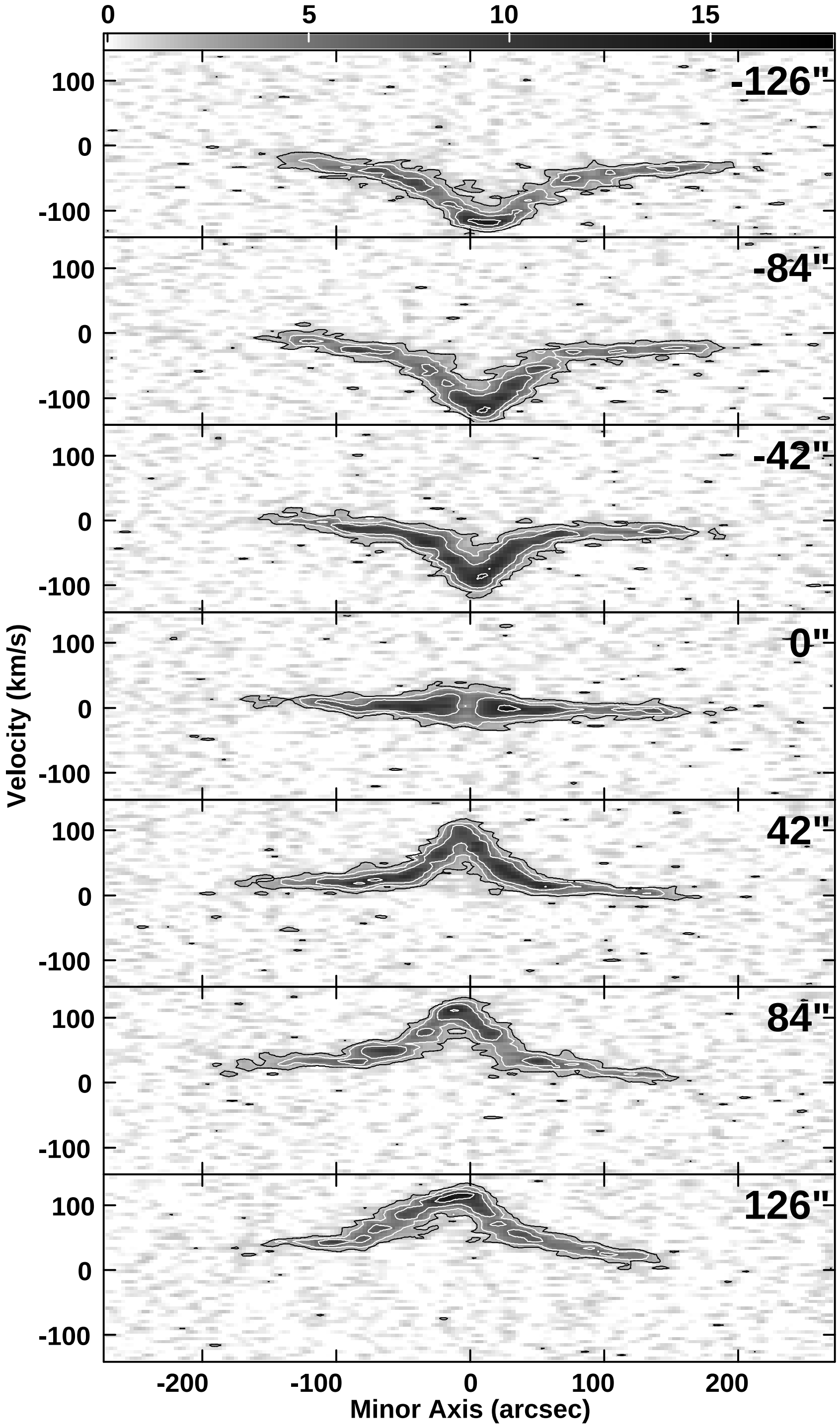


Fig. 5.— Primary-beam corrected images for slices parallel to the minor axis, separated by 42″. Axis labels are relative to the kinematic center and the systemic velocity. The gray-scale is plotted from 0.5 to 18.65 mJy/beam with a logarithmic transfer function and contours are plotted at 1.5, 3, 6, and 12 mJy/beam.

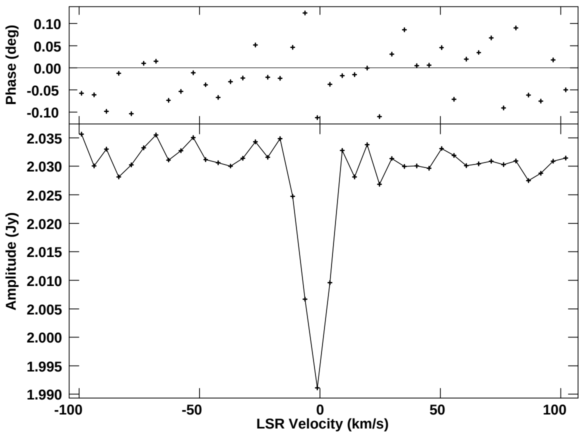


Fig. 6.— The spectrum of calibration source 1800+784 computed by vector averaging all calibrated fringe visibilities.

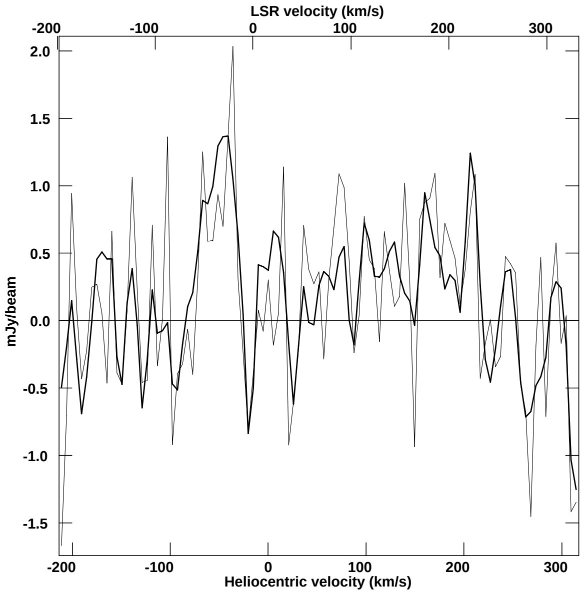


Fig. 7.— The spectrum at the position of 1748+700 (RA = $17^{\mathrm{h}}48^{\mathrm{m}}32\overset{\mathrm{s}}{.}84$, Dec = $+70°05'50\overset{''}{.}8$ in J2000) minus the measured continuum flux density of 755 mJy. Light line from the high-resolution, primary-beam corrected data cube (RMS = 0.58 mJy/beam). Heavy line from a version of the data cube smoothed to $30''$ spatial resolution and 10 km $s^{-1}$ velocity resolution (RMS = 0.38 mJy/beam).

of sight to the quasar passes through the plane of NGC 6503 at a radius of 29 kpc. There must be very little cold HI at this radius in NGC 6503. The absence of absorption from the Milky Way is also remarkable.

We note that in Fig. 7, the peak at an LSR velocity of $\sim -30$ km $s^{-1}$ with a FWHM $\sim 40$ km $s^{-1}$ coincides with the channels contaminated by Milky Way emission over much of the field. The projected heliocentric velocity of the HI disk in NGC 6503 along this line of sight is $\sim 50$ km $s^{-1}$ (LSR velocity of $\sim 65$ km $s^{-1}$); we therefore do not expect Milky Way emission or absorption to confound an absorption signature from NGC 6503.

## 4. HI in NGC 6503: analysis

In this section we examine the HI morphology and kinematics of NGC 6503 in detail.

Analysis of an image over an area much larger than that containing real signal produces large uncertainties due to the inclusion of regions containing only noise. To mitigate this effect in NGC 6503, we produced a cube in which line-free regions were blanked. The multi-scale Cleaned image cube was smoothed in frequency with a Gaussian of 3 channels FWHM and convolved to a spatial resolution of $25''$, producing an image with RMS 0.22 mJy/beam. Then all pixels in the full resolution cube for which the smoothed cube was less in absolute value than three times the RMS of the smoothed cube were blanked. An interactive display program was used to eliminate the remaining pixels throughout the cube that were disconnected from each other and from any region of obvious line signal.

### 4.1. Total HI and its distribution

The blanked image cube may be analyzed along the velocity axis for its zeroth, first, and second moments. The zeroth is a measure of total HI content while the first, if the spectra are narrow and symmetric as they are in NGC 6503, is a measure of the local velocity. Under the same conditions, the second moment reflects the velocity dispersion of the gas. The first two moments are shown in Fig. 8, while the second moment is shown in Fig. 9. In this section, we focus on the features of the zeroth moment map. The HI properties derived from this distribution are summarized in Table 3.

Table 3: Measured properties of NGC 6503

| parameter | value | units | Section |
|---|---|---|---|
| Continuum flux density | $39.4 \pm 0.7$ | mJy | 3.1 |
| Continuum angular diameter | $200 \pm 20$ | arcsec | 3.1 |
| Continuum linear diameter | $5 \pm 0.5$ | kpc | 3.1 |
| Line integral | $205 \pm 1$ | Jy km $s^{-1}$ | 4.1 |
| HI mass | $1.3 \pm 0.2$ | $10^9\,M_\odot$ | 4.1 |
| HI mass / B luminosity | $0.87 \pm 0.13$ | $M_\odot/L_\odot$ | 4.1, 1.1 |
| Integrated line width at 20% peak | 246 | km $s^{-1}$ | 4.1 |
| Integrated line width at 50% peak | 234 | km $s^{-1}$ | 4.1 |
| HI radius ($0.1\,M_\odot$ / $pc^2$) NW | 22.6 | kpc | 4.1 |
| HI radius ($0.1\,M_\odot$ / $pc^2$) SE | 17.2 | kpc | 4.1 |
| Mean HI/optical radius ratio | 3.7 | | |
| Kinematic center (RA, J2000) | $17^h49^m26^s.30$ | | 4.2 |
| Kinematic center (Dec, J2000) | $70°08'40.7''$ | | 4.2 |
| Kinematic Position angle | -60.1 | degrees | 4.2 |
| Inclination | 75.1 | degrees | 4.3 |
| Systemic velocity (heliocentric) | $28.5 \pm 0.3$ | km $s^{-1}$ | 4.2 |
| dynamical mass ($R = R_{max}$= 3.5 kpc) | 1.0 | $10^{10}\,M_\odot$ | 4.2 |
| dynamical mass ($R = 6$ kpc) | 1.8 | $10^{10}\,M_\odot$ | 4.2 |
| dynamical mass ($R = 20$ kpc) | 6.0 | $10^{10}\,M_\odot$ | 4.2 |
| Max. column density[a] | 6.9 | $M_\odot$ / $pc^2$ | 4.3 |
| Max. column density[a] | 8.6 | $10^{20}$ atoms $cm^{-2}$ | 4.3 |
| Minimum detectable signal | 3 | Jy/beam m $s^{-1}$ | 4.1 |
| Minimum detectable column density | $1.8 \times 10^{19}$ | $cm^{-2}$ | 4.1 |

[a]corrected for inclination (75.1°)

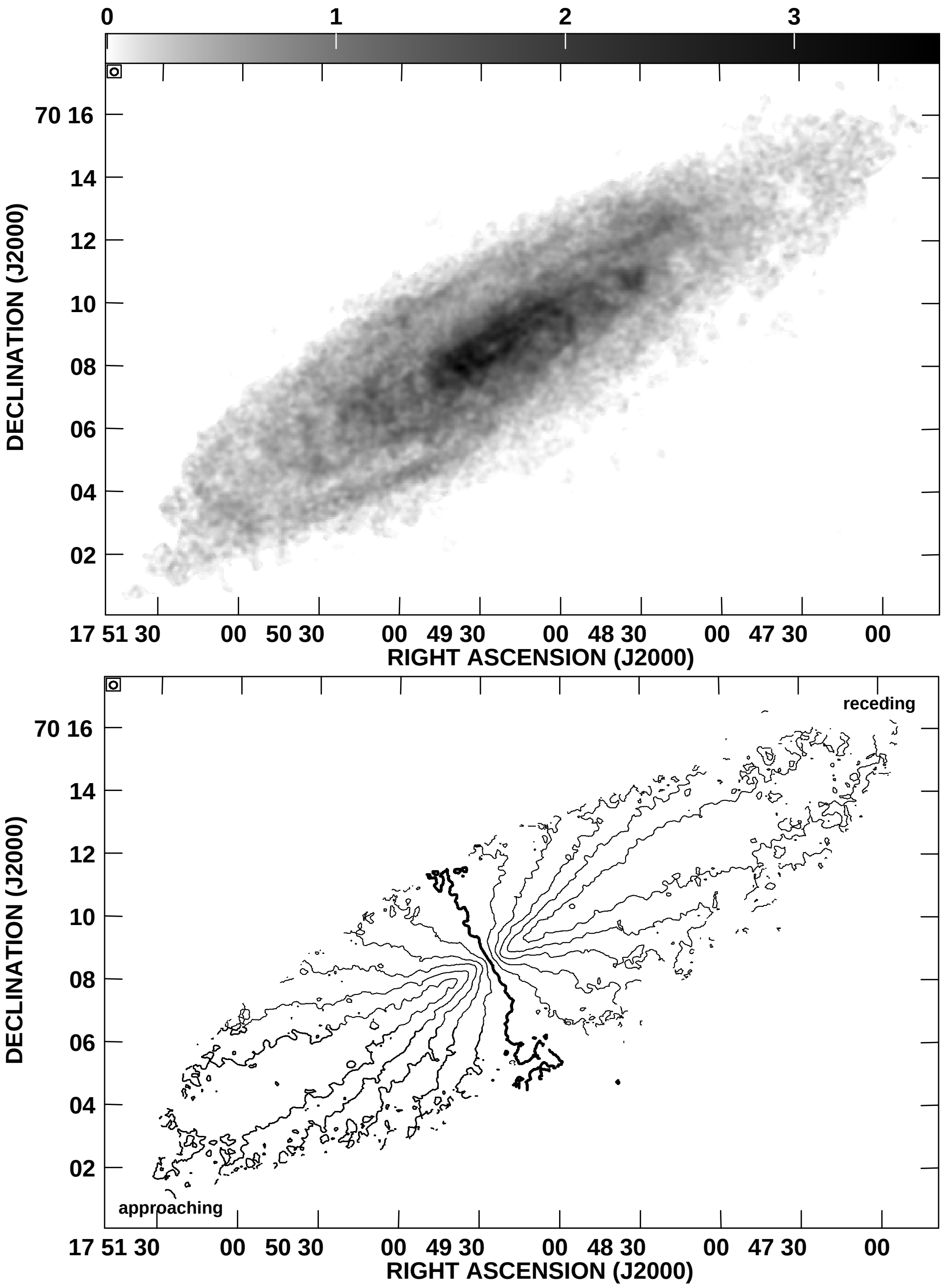


Fig. 8.— Top: zeroth moment of the HI distribution in NGC 6503 measured in $10^{21}\,\mathrm{cm}^{-2}$ and plotted with a logarithmic gray-scale. The column density is $0.57 \times 10^{19}\,\mathrm{cm}^{-2}\,SdV$, with $SdV$ in units of Jy/beam m s$^{-1}$.) The lowest reliable HI emission from NGC 6503 is at $1.8 \times 10^{19}\,\mathrm{cm}^{-2}$. Bottom: first moment of the HI distribution in NGC 6503. The heavy contour is plotted at 26 km s$^{-1}$ heliocentric (nearly the systemic velocity), and the other contours are spaced at 20 km s$^{-1}$ relative to this value. The eastern (E) side is approaching, while the western (W) side is receding.

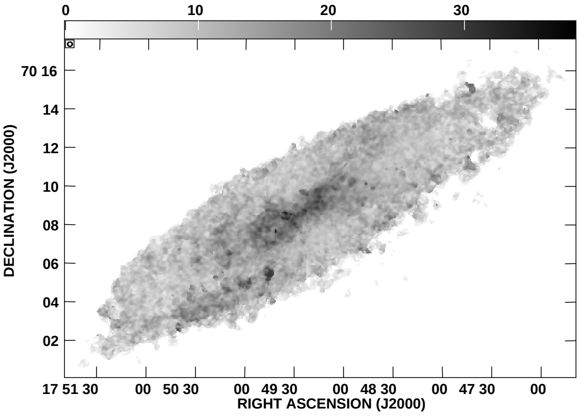


Fig. 9.— Second moment of the HI distribution in NGC 6503 plotted with a linear gray-scale from 0 to 39 km s$^{-1}$. No correction for projection effects has been made.

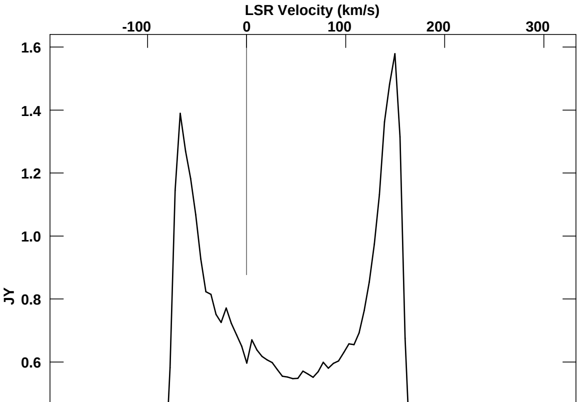


Fig. 10.— The integrated spectrum of NGC 6503 after primary beam correction and blanking of line-free regions. The LSR as well as heliocentric velocities are shown, with a long tick mark at 0 km s$^{-1}$ LSR. Errors in the spectrum due to HI emission from the Milky Way are evident near this velocity.

The weakest pixels in the zeroth moment image in Fig. 8 have values as low as 1 Jy/beam m s$^{-1}$, but the spectra at these pixels do not contain convincingly real line signals even in the smoothed image cube. Convincing line signals are seen at pixels with zeroth moments of 3 Jy/beam m s$^{-1}$, yielding the lowest reliable HI detection from NGC 6503 of $1.8 \times 10^{19}$ cm$^{-2}$.

Integrating over the zeroth moment image yields an integrated flux $S_{\rm int} = 205 \pm 1$ Jy km s$^{-1}$. The corresponding HI mass is given by

$$M_{\rm HI} = (2.356 \times 10^5) S_{\rm int} D^2 \ {\rm M}_\odot \ , \qquad (1)$$

where $S_{\rm int}$ is in Jy km s$^{-1}$ and $D$ is the distance to NGC 6503 in Mpc. The total HI mass of NGC 6503 is therefore $M_{\rm HI} = 1.3 \pm 0.2 \times 10^9 \ {\rm M}_\odot$, including a 10% uncertainty in $D$. The integrated spectrum of NGC 6503, obtained by summing the flux in each channel of the blanked image cube, is shown in Fig. 10 and yields the same HI mass within the uncertainties. The width of the integrated profile is $W \sin i = 234$ km s$^{-1}$ at the half-peak points (246 km s$^{-1}$ at 20% points).

Several features should be noted in the zeroth moment image in Fig. 8. The first is the appearance of spiral structure, particularly in the outer parts of the disk. The approaching arm along the southeastern (SE) edge is particularly prominent. Other arms are visible in the interior to the SE, NE, and NW. The spiral arms also appear conspicuously in residual images after fits to a smooth HI distribution by CUBIT (Section 4.3 and Fig. 13). Note that, if the spiral arms are trailing arms in the usual sense, the southern edge of NGC 6503 is closer than the northern edge.

There are also a number of holes in the HI distribution in Fig. 8, where a distinct minimum is surrounded by a ridge of HI. One of these is at the very center of the NGC 6503 with an apparent FWHM of 20″. Deconvolved from the beam, this diameter is about 14″ or 0.35 kpc. This hole is visible in the channel and transposed images of Figs. 3 through 5. Presumably either the neutral hydrogen has been converted to molecular form or it has been ionized or evacuated by the activity at the center of the galaxy which gives rise to the weak continuum radio source. South of the center there is another clear depression with an apparent width of 17″, or a deconvolved width around 0.24 kpc. Such HI bubbles are seen in other nearby galaxies:

for example, detailed observations of M33 reveal a multitude of these holes (Thilker, Braun, & Walterbos 2002) which appear to be correlated with large OB associations (Deul & den Hartog 1990).

Shostak, Willis, & Crane (1981) found that NGC 6503 is considerably more extended to the SE than to the NW, with 1.25 times more HI on the E or approaching half. Measuring the zeroth moment image in some detail, we do not confirm these early results. Instead we find that the average HI in the approaching half is about 11% more per pixel but over 8% fewer pixels. The net is only 4% more HI in the approaching side of the galaxy. The outer major axis radius to the NW is 900″ (22.6 kpc), while it is only 825″ (17.2 kpc) to the SE.

The mean HI/optical radius ratio is therefore 3.7 for NGC 6503. While this value is larger than typically observed in spirals (Broeils & Rhee 1997), it does not rival the relative HI extents of some low-mass systems (e.g. Gentile et al (2007)).

### 4.2. Kinematics

The first moment of the HI distribution in Fig. 8 shows that the kinematics of NGC 6503 are highly regular. We find some evidence for a mild warp in the outer disk, first identified by Shostak, Willis, & Crane (1981): the isovelocity contours in Fig. 8 make a somewhat greater angle with the major axis in the NE and SW quadrants compared to the NW and SE ones. The emission in some individual channels of the image cube exhibits the same behavior, notably at -10.1 km s$^{-1}$ and 67.2 km s$^{-1}$ in Fig. 3.

The second moment image (Fig. 9) has larger values toward the center of the galaxy where the steepness of the rotation curve produces an increase in the line width due to the finite beam width. There is also a quite noticeable peak in the second moment near where the SE arm bends abruptly. That feature is due to the presence of a second spectral feature in that area, slightly offset in velocity from the main feature; see the emission at -54.4 km s$^{-1}$, -41.0 km s$^{-1}$ and -25.5 km s$^{-1}$ in Fig. 3. It is plausible that the bend in the isovelocity contours in the first moment at that location (Fig. 8) also stems from this limited spectral feature.

Van Moorsel & Wells (1985) describe an AIPS

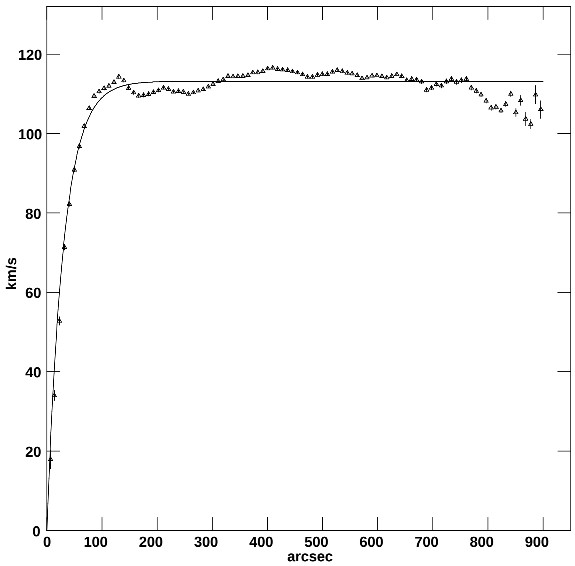


Fig. 11.— Rotation curve for the HI disk of NGC 6503, obtained from the AIPS program GAL by fitting all points in the first moment image.

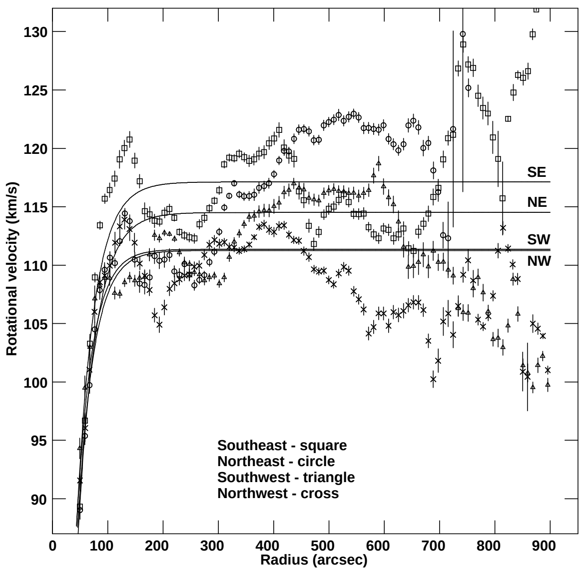


Fig. 12.— The rotation curve fit by the GAL program for the NW (cross symbols), SW (triangles), NE (circles), and SE (squares) quadrants. Note that the velocity tick marks are separated by about one spectral channel in this blown-up display.

program GAL which fits rotation curves to user-selected portions of the first moment image with optional weighting by the zeroth moment image. We first used GAL to model the kinematics of the NGC 6503 HI disk as a whole: after fitting for the kinematic center of the disk, this value was held fixed and the position angle of the receding major axis and the systemic velocity were derived. The best fitting values for these parameters are given in Table 3. Holding these parameters fixed, we then proceeded to fit for the inclination and the rotation curve of the system using the functional form:

$$V = V_{\max}\left(1 - e^{-\ln(100)R/R_{\max}}\right) \qquad (2)$$

where $V_{\max}$ is the maximum velocity of the rotation curve, which occurs at a radius $R_{\max}$.

The rotation curve obtained by fitting all points in the first moment image is given in Fig. 11, and the extracted parameters are given in the first row of Table 4. The rotation curve in Fig. 11 rises out to $R = 140''$ (3.5 kpc), and then remains flat out to $R = 770''$ (19.4 kpc). There is some evidence for a decrease in rotation amplitude beyond this, out to the last measured point at $R = 900''$ (22.6 kpc). Given a rotation curve, the dynamical mass enclosed within a radius $R$ can be computed assuming spherical symmetry:

$$M_{\rm T} = (2.325 \times 10^5) R\, V_{\rm rot}^2\ M_\odot\ , \qquad (3)$$

where $R$ is in kpc, and $V_{\rm rot}$ is the rotation curve amplitude in km s$^{-1}$ measured at $R$. Dynamical mass estimates at different $R$ for the rotation curve in Fig. 11 are given in Table 3.

We then extracted the rotation curves and inclinations of NGC 6503 in the NW, NE, SW and SE quadrants of the disk defined by the kinematic major and minor axes. The results from these fits are shown in Fig. 12 and Table 4. Despite the regularity of the first moment image for NGC 6503, the discrepancies between the best fitting parameters for each quadrant suggests the presence of non-circular motions and geometric distortions in the disk. The SW quadrant inclination differs from the NW by 2.6 degrees in the direction of the plane bending down in that quadrant. The eastern side, however, gives an intermediate inclination which is the same in both quadrants, failing to confirm the second half of the warp suggested above. We note that the velocities and physical dimensions in the eastern half are somewhat larger than in the western half. Fig. 12 makes it clear that there are small-scale deviations, of order plus/minus one spectral channel (5 km s$^{-1}$), from simple rotation in all four quadrants. The deviations are greatest in the SE and NW in which the view is along spiral arms against the direction of motion in the SE and in the direction of motion in the NW. Peculiar velocities due to spiral structure would be expected in those locations.

Table 4: GAL fit parameters by quadrant

| quadrant | inclination<br>deg | $V_{\max}$<br>km s$^{-1}$ | $R_{\max}$<br>arcsec |
|---|---|---|---|
| all | 72.6 | 113.2 | 139.2 |
| SW | 71.7 | 111.4 | 129.7 |
| NW | 74.3 | 111.3 | 135.5 |
| NE | 72.7 | 114.5 | 149.9 |
| SE | 72.3 | 117.1 | 145.7 |

### 4.3. CUBIT models

Another AIPS task, CUBIT, was initially developed by Irwin (1994) to fit the entire data cube rather than just the first moment image. The model assumes that the galaxy is a disk of finite thickness in circular rotation, and fits for one of several functional forms of the HI density distribution and rotation curve. The CUBIT model fit to NGC 6503 held the kinematic center and systemic velocity fixed to the values in Table 3 while fitting for a Gaussian density profile within the plane of the disk, an exponential density profile perpendicular to the plane, and a Brandt rotation curve given by

$$V(R) = \frac{V_{\rm B}\, R/R_{\rm B}}{\left(\,1/3\ +\ 2/3(R/R_{\rm B})^m\,\right)^{3/(2m)}} \qquad (4)$$

where $V_B$ and $R_B$ characterize the rotation curve shape and $m$ is the "Brandt index." The results of the CUBIT fits to the NGC 6503 cube are summarized in Table 5, where the columns labeled "minimum" and "maximum" illustrate the range in parameter values found when CUBIT is restricted to different regions of the disk. In general, there is good agreement between the best fitting parameters found by GAL (Table 4) and by CUBIT (Table 5). We note that a higher inclination is ex-

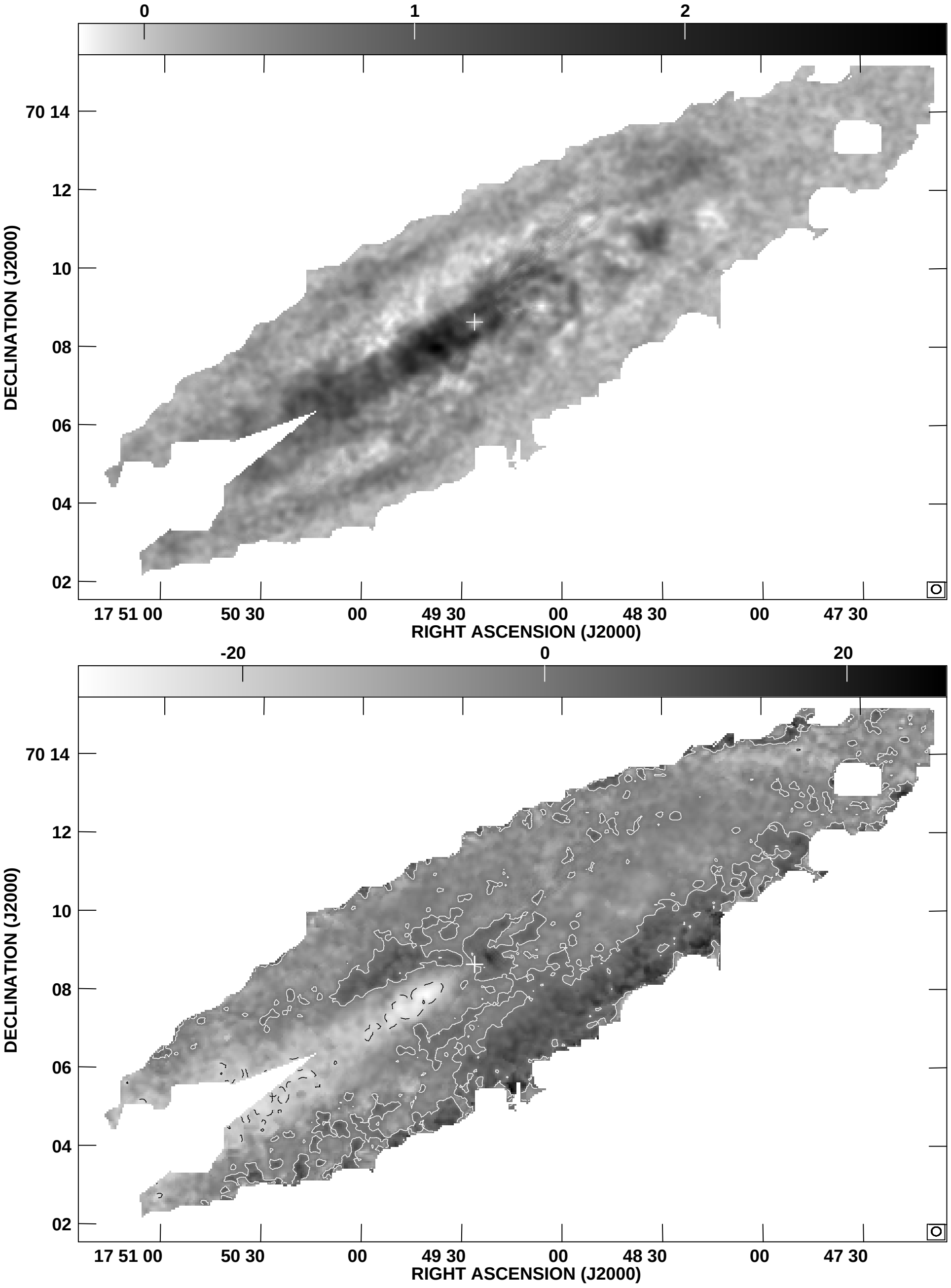


Fig. 13.— Top: zeroth moment image of NGC 6503 minus that fit by CUBIT plotted with a logarithmic gray-scale. The step wedge is marked in steps of $10^{21}\,\mathrm{cm}^{-2}$. A comparison of the CUBIT model and the radial column density along the major axis is shown in Fig. 14. Bottom: first moment image of NGC 6503 minus that fit by CUBIT. The white contour is drawn at 0 km $\mathrm{s}^{-1}$, and the black, dashed contour is drawn at -20 km $\mathrm{s}^{-1}$.

Table 5: Fit parameters from CUBIT

| parameter | units | full galaxy | minimum | maximum |
|---|---|---|---|---|
| Position angle | degrees | -60.3 | -62.4 | -58.2 |
| Inclination | degrees | 75.1 | 73.5 | 76.0 |
| $V_B$ | km s$^{-1}$ | 118.7 | 118.3 | 119.9 |
| $R_B$ | arc sec | 172.6 | 168.5 | 218.7 |
| Brandt index | | 0.091 | 0.060 | 0.69 |
| Maximum density | cm$^{-3}$ | 0.147 | 0.134 | 0.180 |
| Radial density scale[a] | arcsec | 353.5 | 329.2 | 373.3 |
| Vertical density scale[a] | arcsec | 26.0 | 23.6 | 33.0 |
| Vertical column density | $10^{20}$cm$^{-2}$ | 4.1 | 4.1 | 4.8 |

[a]the radius or height at which the density falls by a factor of $1/e = 0.3679$.

pected from CUBIT, since GAL assumes a thin disk while CUBIT takes its finite thickness into account.

Fig. 13 shows the residuals when the best fitting CUBIT model for the disk as a whole is subtracted from the data. The residuals emphasize the geometric and kinematic deviations from an ideal disk that were discussed in Sections 4.1 and 4.2. They are largest along the SE major axis, where the CUBIT model greatly underestimates the zeroth moment and does not fit the velocity profile well. The kinematic discrepancy between the data and the model might be expected given the rotation curve fits in Fig. 12, where the largest disparity between the quadrants within the optical radius is between the SE and SW at $R \sim 130''$. The first moment velocities in the data also exceed the model by up to 20 km s$^{-1}$ along the southern edge. This provides some support for the previous suggestion of a warp in the SW.

Integrating the exponential vertical density profile, the CUBIT model provides the best fit Gaussian to the radial column density profile in NGC 6503. This profile can also be estimated directly from the zeroth moment image. Different inclination-corrected measures of the radial column density in NGC 6503 are shown in Fig. 14, where the plus signs show the CUBIT model output, the squares show the profile obtained by averaging concentric rings in the zeroth moment image, and the dashed and solid lines show the profiles obtained from slices of the zeroth moment image along the major axis to the SE and NW,

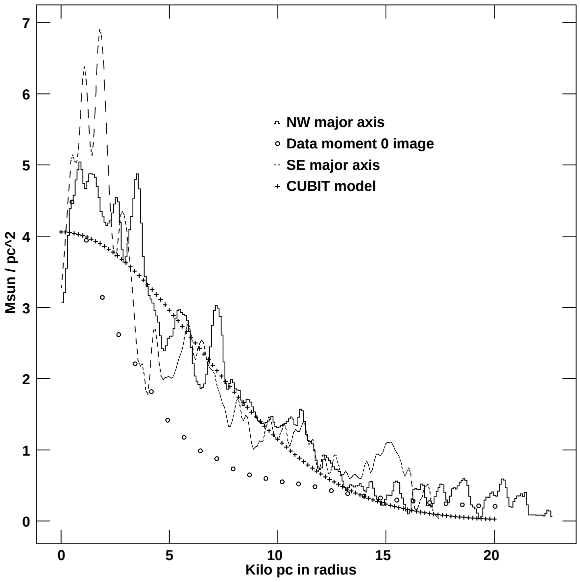


Fig. 14.— The radial column density in $M_\odot/pc^2$ plotted against radius in NGC 6503. The plus signs trace the CUBIT model, the squares are averages over concentric rings in the zeroth moment image, and the dashed and solid lines are slices in the zeroth moment image along the major axis to the SE and NW, respectively. The slices have been corrected to radial column densities by multiplying by the cosine of the inclination (75.1°).

respectively. A comparison between the CUBIT model output and the SE and NW major axis profiles explains the large zeroth moment residuals in Fig. 13: the surface density profile is well-approximated by a Gaussian along the NW major axis, but deviates from this functional form by almost a factor of two along the SE major axis at $R \sim 2\,\mathrm{kpc}$ ($80''$). As a result, the zeroth moment residuals in Fig. 13 contain nearly 45% of the total HI in NGC 6503. We note that the radial column density profile estimated from the zeroth moment image is contaminated by the relatively poor resolution along the minor axis due the high inclination of NGC 6503: this biases the profile low at intermediate $R$ and high at large $R$.

The peak column densities and other parameters found here are similar to those found by van der Hulst et al. (1993) for a number of low surface brightness galaxies. Like them, NGC 6503 falls below the average for field Scd galaxies (8.5 $\mathrm{M}_{\odot}\,/\,\mathrm{pc}^2$) and would fall below the Kennicutt (1989) criterion for normal star formation.

### 4.4. Extra-planar HI Models

In comparison to the HI distributions of several nearby spirals (Fraternali et al. 2002; Matthews & Wood 2003; Boomsma et al. 2005; Oosterloo, Fraternali, & Sancisi 2007), position-velocity slices along the major (Fig. 4) and minor (Fig. 5) axes of NGC 6503 show little evidence for low-velocity gas and a high degree of symmetry, respectively. Our CUBIT models of NGC 6503 (Section 4.3) suggest that the mean vertical density scale[1] of its HI layer is $26''$ (0.65 kpc). Taken together, the position-velocity slices and CUBIT models thus suggest that NGC 6503 lacks the thick, lagging extra-planar HI layer that is commonly detected in spiral galaxy observations at this sensitivity (see Section 1 for references). In this section, we model the vertical extent and kinematics of the HI layer in NGC 6503 to place quantitative constraints on the properties of its extra-planar gas.

To emphasize any large-scale, low column-density features that might be present in the data, we smoothed the HI cubes presented in Section 3.2 spatially and spectrally to a resolution of $30''$ and $10.3\,\mathrm{km\ s^{-1}}$. We compare our models to this smoothed cube.

We use the GIPSY (van der Hulst et al. 1992) task GALMOD to model NGC 6503 as one or two HI layers of finite thickness in circular rotation, using the results from the analysis in Sections 4.2 and 4.3 as inputs. In all of the models, we adopt a kinematic center, position angle and systemic velocity identical to the values in Table 3 and a constant velocity dispersion of 8 km $\mathrm{s}^{-1}$ (Fig. 9).

Our CUBIT models suggest that the receding (W) side of the disk is better approximated by a smooth HI layer than the approaching (E) side (Fig. 13), and we therefore focus on reproducing its properties with GALMOD. Specifically, the input model kinematics are the rotation curve extracted by GAL for the receding half of the disk, and the input HI surface mass density is that along the NW major axis (Fig. 14). We have corrected the input rotation curve and HI surface density for beam smearing at $R < 100''$. The output models are smoothed to the same spatial and spectral resolution as the smoothed data cube.

A selection of galaxy models is compared to the smoothed NGC 6503 image cube in Fig. 15. The left column shows a position-velocity slice along the NW major axis, and the right column shows the detected HI emission in the channel at $V = 103.3\,\mathrm{km\ s^{-1}}$. The contours in all rows of a column are identical. We choose to show these model properties because we find that they provide the best diagnostics of the vertical extent and kinematics of the HI layer. We note that because of projection effects there was little difference between the position-velocity slices along the minor axis for various models, and they are not included in Fig. 15.

We first model the HI in NGC 6503 as a single Gaussian layer. Figs. 15b and 15c show the model morphologies for HI layers with FWHM = 0.5 kpc and FWHM = 4.5 kpc, respectively. They illustrate that a model with a thin HI layer (Fig. 15b) reproduces the gross features of the major axis position-velocity slice beyond the optical radius ($R = 3.55'$) as well as the observed channel maps: this is expected given the low vertical density scale returned by CUBIT (Section 4.3). However, this model is unable to reproduce the position-velocity contours within the optical disk: there is more anomalously low-velocity gas at these radii than

[1] height over which the density drops by a factor of $1/e = 0.3679$

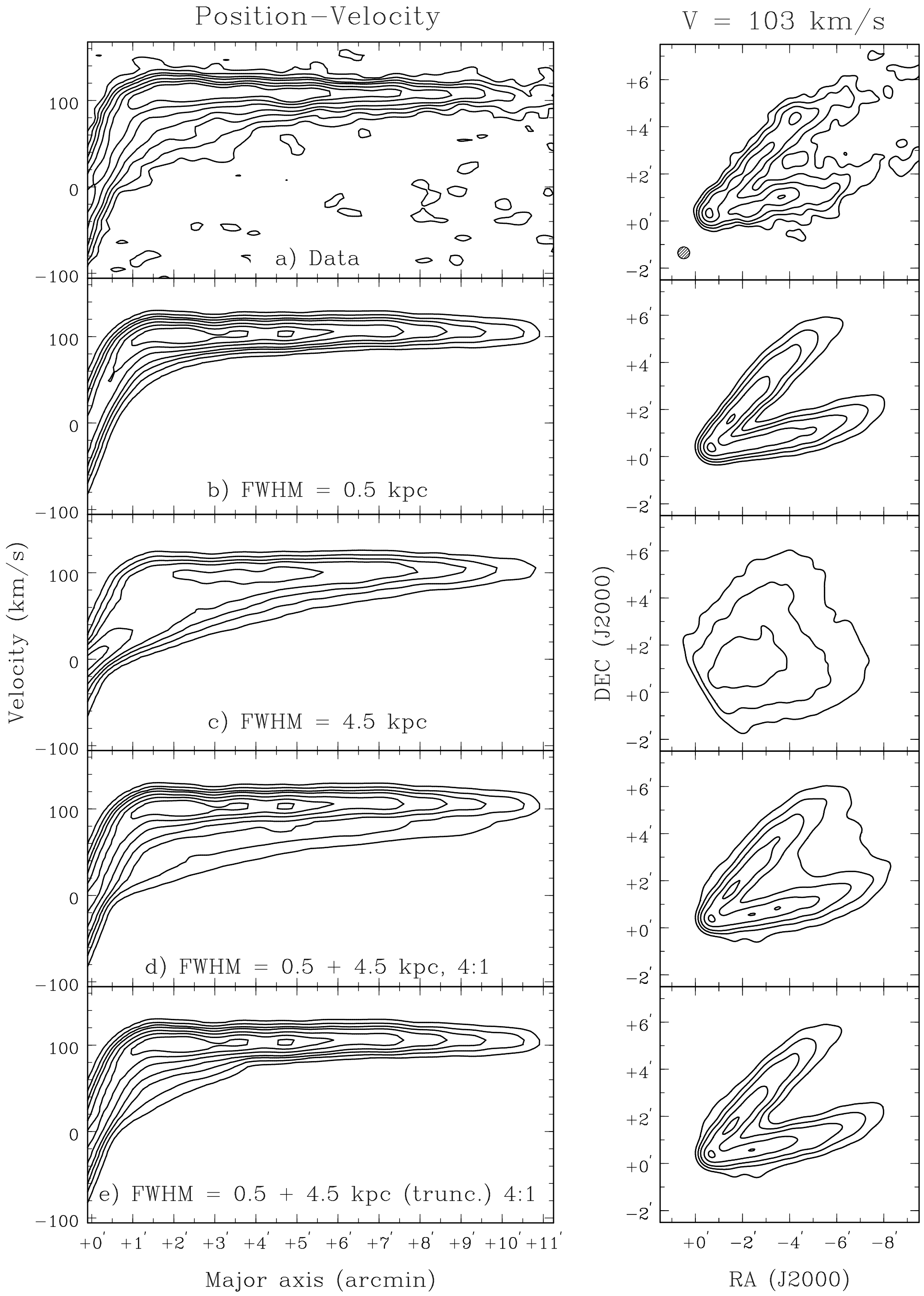


Fig. 15.— Position-velocity slices along the NW major axis (left) and channel map at $V = 103.3\,\mathrm{km\ s^{-1}}$ (right) in a) the smoothed image cube, and b) – e) various GALMOD models. The contours in the position-velocity panels are at $(1, 3, 6, 10, 18, 28, 40) \times 0.76$ mJy/beam, and the contours in the channel map panels are at 1.5, 4 ,8 ,16 and 24 mJy/beam. Panels b) – e) show our most plausible models including b) a single thin HI layer, c) a single thick HI layer, d) thin and thick layers with a column density contrast of 4:1 where the thick disk lags the thin one by $25\,\mathrm{km\ s^{-1}}$, e) thin and thick layers with a column density contrast of 4:1 where the thick disk lags the thin one by $25\,\mathrm{km\ s^{-1}}$ and is truncated at the optical radius ($R = 3.55'$).

expected. Fig. 15c demonstrates that invoking a thick HI layer does produce low-velocity gas at small $R$ in the position-velocity slice, but that both the model channel map and position-velocity morphologies are inconsistent with the data.

We thus proceed to model NGC 6503 with both a thin and a thick layer. As in Schaap, Sancisi, & Swaters (2000), we find that plausible models with co-rotating thick and thin layers have similar morphologies to our one-component models. We therefore explore models where the thin and thick layers have the same column density profile shape and rotation profile shape, but where the thick layer has a total column density and rotation velocity that are lower than that in the thin layer.

Fig. 15d shows one of our better models of NGC 6503 with this morphology. The thin layer has a FWHM of 0.5 kpc. The thick layer has a FWHM of 4.5 kpc, and rotates 25 km s$^{-1}$ slower at all $R$ compared to the thin disk. The thin:thick layer column density ratio is 4:1. We see that the morphology of the position-velocity slice within the optical disk approaches that seen in the data. However, the model also predicts detectable low-velocity gas at larger $R$ in the position-velocity slices as well as large-scale, low-intensity emission in the channel maps which are not observed in the data. Increasing the column density ratio between the HI layers alleviates the discrepancies in the outer disk and channel maps, but the models then fail to reproduce the "beard" across the optical disk for plausible differences in velocity between the layers. We therefore find that this class of models, too, fails to reproduce the position-velocity slice and channel map morphology at all locations in the HI disk.

Finally, we invoke 2-component models where the thick, low column-density, lagging HI layer is truncated beyond the optical radius. One of our better models with this morphology is shown in Fig. 15e. The thick layer has a FWHM of 4.5 kpc, and rotates 25 km s$^{-1}$ slower at all $R$ compared to the thin disk. Within the optical radius ($R = 3.55'$), the thin:thick layer column density ratio is 4:1, and the thick layer has zero column density farther out. This model is the only one in Fig.15 that reproduces the morphology of the major axis position-velocity slice as well as the channel maps. While not shown here, this is also the case for the advancing half of the disk, as well as for other channels and slices in the cube.

Given the sensitivity of our data, we estimate that truncated 2-layer models with combinations of column density ratios between 4:1 and 6:1, velocity lags between 20 km s$^{-1}$ and 40 km s$^{-1}$, and thick layer FWHM between 3 kpc and 5 kpc could reproduce the data. However, the column density ratio between the thin and thick disks outside the optical disk must be $\gtrsim$10:1 in order to escape detection at the 3-5$\sigma$ level. We therefore conclude that the extra-planar HI layer in NGC 6503 extends only out to its optical radius.

## 5. Discussion and conclusions

We have presented aperture synthesis observations of the nearby, late-type spiral galaxy NGC 6503. Advances in calibration and imaging software enabled us to produce a wide-field continuum image at a dynamic range of 9000:1. We detect HI emission at column densities as low as $1.8 \times 10^{19}$ cm$^{-2}$, with a spatial resolution of 0.35 kpc at the galaxy (Fig. 8): our images thus have 7 and 6 times higher sensitivity and resolution than those of van Moorsel & Wells (1985), respectively. The HI cube is also to a great extent free of contamination due to missing short spacings. In Appendix A, we discuss the improved imaging algorithms available within the AIPS software package which have made these images possible.

Even at the higher sensitivity and resolution of our observations relative to previous studies, we find that the HI disk in NGC 6503 is remarkably regular (Figs. 3, 8). Nonetheless, several deviations from an idealized distribution are apparent: the outer portions of many emission "wings" bend away from the major axis in the channel maps, and the zeroth moment reveals a number of density enhancements giving the impression of large-scale spiral arms as well as smaller spiral-like structures closer to the dynamical center. The HI density is reduced at the dynamical center and at several other locations in poorly-resolved holes about 0.3 kpc in diameter.

We trace the rotation curve of NGC 6503 out to 3.7 optical radii (Fig. 11), and find that it is flat almost out to the last measured point. Fitting rotation models to the first moment image by quadrants reveals kinematic features comparable in size to the channel width (5.15 km $s^{-1}$), some of which probably reflect spiral density wave disturbances (Fig. 12). This is also evident in our CUBIT models of the HI density distribution and kinematics (Fig. 13): the velocity field is distorted from the fit model in the SW portion of NGC 6503, partially confirming the presence of the warp in the plane suggested by Shostak, Willis, & Crane (1981). However, a comparable disturbance to the kinematics is not observed on the opposite side of the plane. In addition, the HI density is greatly enhanced compared to, with a significant velocity discrepancy from, the fit model along the SE major axis. Careful consideration of these asymmetries will be taken in forthcoming dynamical models.

Despite the greater HI emission-line sensitivity of some recent observations of nearby spirals compared to those presented here (e.g. Fraternali et al. 2002; Oosterloo, Fraternali, & Sancisi 2007), we find that the disk of NGC 6503 extends to a similar limiting column density (Fig. 8). In the images of Fraternali et al. (2002), the disk of NGC 2403 truncates at $\sim 2 \times 10^{19}\,\mathrm{cm}^{-2}$ (see their fig. 6), and the lowest contour in the Oosterloo, Fraternali, & Sancisi (2007) map of NGC 891 is at $1.0 \times 10^{19}\,\mathrm{cm}^{-2}$ (see their fig. 1; they do not discuss an actual examination of the spectra at such points). We trace the HI disk in NGC 6503 out to $1.8 \times 10^{19}\,\mathrm{cm}^{-2}$ (22.6 kpc). But the absence of absorption towards the quasar 1748+700 yields an upper limit of $5 \times 10^{17}\,\mathrm{cm}^{-2}$ for the column density of cold HI gas along a line of sight which should intersect the disk at 29 kpc (Fig. 7). Our results therefore support the remark by Oosterloo, Fraternali, & Sancisi (2007) that significant improvements in sensitivity have not increased the observed radial size of HI disks. Perhaps we are observing the cutoff suggested by Silk & Sunyaev (1976) due to ionization by an intergalactic UV radiation field.

While disks do not "grow" radially when observed at higher sensitivity, nearly all exhibit extra-planar HI at lower velocities than those in the plane of the disk (see Section 1 for references). Our images, when smoothed to achieve greater sensitivity, are no exception (Fig. 15). We model the vertical extent and kinematics of this extra-planar HI, and find that the channel maps and position-velocity images of NGC 6503 are best described by 2-component models with a thin disk and a low column density, lagging thick disk that is truncated at the optical radius. We estimate that 2-component models with combinations of thin:thick layer column density ratios between 4:1 and 6:1, velocity lags between 20 km $s^{-1}$ and 40 km $s^{-1}$, and thick layer FHWM between 3 kpc and 5 kpc could reproduce the data. However, the thin:thick column density ratio beyond the optical radius must be $\gtrsim 10:1$ for consistency with our images.

There is therefore a clear correlation between the presence of extra-planar gas in NGC 6503 and its stellar disk. This morphology is hard to reconcile with models in which accreting gas forms the thick HI disk (Barnabè et al. 2006; Kaufmann et al. 2006). NGC 6503 therefore provides clear evidence for a galactic fountain origin for most of the extra-planar gas in nearby galaxies, as suggested by the models of NGC 2403 and NGC 891 by Fraternali & Binney (2008). If 10–20% of the extra-planar gas does stem from accretion as suggested by Fraternali & Binney (2008), it may be possible to detect its interaction with the *thin* disk beyond the optical radius of NGC 6503. Considering our limits on the column density ratio between the thick and thin layers, observations with 2–3 times the sensitivity of those presented here would be needed to detect this phenomenon. Such sensitive observations would also allow for a detailed search of High Velocity Cloud analogs in a galaxy with a modest star formation rate, which may shed some insight into their origin as well.

The authors would like to thank Miller Goss for his encouragement and many helpful comments on this manuscript. EWG also had useful discussions with Juan M. Uson, Morton S. Roberts, and David E. Hogg. KS acknowledges support from a research grant from the National Sciences and Engineering Research Council of Canada.

The National Radio Astronomy Observatory is a facility of the (U.S.) National Science Foundation operated under cooperative agreement by Associated Universities, Inc.

NRAO(VLA)

## A. Image Deconvolution in IMAGR

The imaging and deconvolution of most data collected by the VLA are performed with the AIPS task IMAGR. Since a number of algorithms within this program have a significant impact on the quality of the resulting images, we elaborate on its functionality here. We focus on the multi-scale Clean implementation in IMAGR, and illustrate some of its advantages over the standard point-source Clean using the NGC 6503 data presented in this paper. A similar implementation of the multi-scale Clean is described by Cornwell (2008) and an extensive study of its use in imaging HI in galaxies has been described by Rich et al. (2008). Their conclusions regarding this method are similar to ours.

### A.1. Cotton-Schwab-Clark Clean

Clean was proposed by Högbom (1974) as a method to determine the sky brightness distribution of an object from incompletely sampled visibilities. A review of Clean and its variants can be found in Cornwell, Braun & Briggs (1999); briefly, a suite of suitable models are convolved by the beam synthesized from the visibility data and iteratively subtracted from an image until a user-specified criterion is reached. The model components are then convolved with a "Clean" representation of the synthesized beam (typically a Gaussian) and added back into the residual image to form the sky brightness distribution.

When the Clean algorithm works solely in the image domain, the convolution of the model with the synthesized beam must be carried out over an area four times larger than that to be Cleaned. Clark (1980) pointed out that a smaller "beam patch" could be used to find a modest number of model components, after which the residual image could be re-computed by subtracting the current source model fully. This image-based Clark Clean did the subtraction via Fourier transforms of images. Cotton and Schwab (see Schwab 1984) were the first to suggest and implement an extension of this method. In the "Cotton-Schwab-Clark" version of Clean, after the modest number of model components are found, their visibilities are subtracted from the residual visibility data and a new residual image is formed; the process then continues. This allows model components to be found over most of the image while avoiding Fourier transform aliasing and other inaccuracies in the model subtraction. Cumulative computational error in the imaging is also reduced since the images are continually recomputed using the current residual data which gradually approaches the noise levels. The Cotton-Schwab-Clark Clean is the default deconvolution algorithm in IMAGR.

Unconstrained, the Clean algorithm can move flux density from real objects into erroneous locations (Condon et al. 1998). The synthesized beam of well-sampled visibility data from the VLA reduces this "Clean bias," because of the relatively low sidelobe levels. To reduce it further, Cleans are typically restricted interactively ("boxed") to those areas clearly containing real emission. Any emission regions too weak to be included will have negligible sidelobes and, thus, do not need to be deconvolved. We compare the flux densities measured from images deconvolved with unrestricted and boxed Cleans for the particular case of NGC 6503 in Appendix A.4.

### A.2. Wide-field imaging

When images are constructed with two-dimensional Fourier transforms from interferometers that are not co-planar, errors occur which increase as the square of the angular distance from the phase reference point. In order to avoid serious distortions in source shapes and coordinates, images of large areas must be made up of rather smaller facets (Cornwell & Perley 1992). The choice of facet location is significant, since aliasing and other numerical errors render the edges and, especially, the corners, of images unreliable. AIPS implements an algorithm due to W. D. Cotton in which the facets are placed on circles so that the full area may be Cleaned without using the facet corners.

When imaging a particular facet, IMAGR rotates the projected baseline coordinates and the observed phases to the phase reference position at the facet center. An inverse rotation is performed when the model components in the facet are subtracted from the current residual data. These rotations are simple matrix multiplications and and generally have a negligible computational cost. Additionally, the time required to deconvolve correctly-rendered emission is considerably less than that required to attempt to deconvolve distorted renderings. The computed synthesized beam varies slightly from facet to facet. IMAGR differs from other faceting implementations in that it selects one facet to be Cleaned in the current cycle, finds new model components in that facet, and subtracts them from the current residual data. When it selects the next facet to Clean (see Section A.3), it re-images that facet using the latest residual visibility data. In this way, sidelobes of a strong source in one facet are therefore removed from the others before the latter are Cleaned, which avoids a significant bias in the final image that is otherwise hard to mitigate.

### A.3. Multi-scale Clean in IMAGR

Clean was originally described as a method to model a sky brightness distribution as a collection of point sources (Högbom 1974). While a point-source Clean deconvolves poorly-resolved objects accurately and efficiently, it requires a large number of components to represent more extended objects and those representations can have non-physical attributes (e.g., Cornwell 1983). In particular, Clean has a bias against pixels adjacent to one recently selected. To mitigate artifacts in the final image from this bias, model objects are restored to the residual image only after convolution with a "Clean beam." Nonetheless, images of extended objects deconvolved with a point-source Clean tend to show systematic corrugations that can be confused for real structure (e.g., Cornwell, Braun & Briggs 1999).

As early as 1974, one of us (EWG, unpublished) began investigating the use of Gaussian source models in the Clean algorithm instead of point-source models. Extended sources of a single size cannot accurately model point sources, however, and are of little interest in an astronomical context since most fields contain unresolved objects. In order to mitigate these difficulties, Wakker & Schwarz (1988) developed an image-based algorithm which simultaneously solved for point components *and* Gaussians of a single pre-determined size. Holdaway & Cornwell (1999) described an extension of this algorithm which would model the image with Gaussians of a few selected widths as well as with points. Their algorithm was an image-only Clean with "cross beams" for subtracting components of one scale from images made for another scale. At each iteration, a component was found in the sky brightness distribution imaged on a particular scale, and then subtracted from the distributions imaged on all scales. It was said that this algorithm could run with high loop gain[2] and almost no user-set steering parameters.

The multi-scale Cotton-Schwab-Clark Clean implemented in IMAGR is rather different from the Holdaway & Cornwell (1999) algorithm, and has now been successfully applied to a number of datasets (e.g. Thilker, Braun, & Walterbos 2002; Clarke & Ensslin 2006; Monjian et al. 2006; Kent et al. 2008). The user specifies the number of circular Gaussians to be used as model components, as well as their widths. Although it is not required, one of these Gaussians should have a width of zero to model unresolved objects and other small-scale structures accurately. IMAGR converts these widths into tapers (Gaussian functions which lower the weights at larger projected baseline lengths) for each scale and uses them to make images of the beam and the data. These tapered beam images are used to correct the data images to units of Jy/beam and to determine the Gaussian Clean beam for each scale. IMAGR then discards the beam images and constructs new beam images at each scale representing the convolution of the tapered beam with the Clean beam. This process is carried out rather simply by re-making each beam image with a taper $\sqrt{2}$ smaller, where the taper parameter in AIPS is the baseline length at which the tapering Gaussian function reaches 30%.

IMAGR Cleans each resolution for each facet separately, treating $M$ spatial facets times $N$ scales as $MN$ total facets. At each major cycle, it selects one of the $MN$ facets to Clean, images that facet with the current residual visibility data, finds Clean components in that facet, and subtracts the Fourier transform of those components from the residual visibility data. It stops Cleaning a particular facet when the peak flux density therein falls below a scale-dependent cutoff, and the cleaning stops altogether when all facets satisfy this or another termination criterion. The components on all scales are then restored to the image made at the finest (usually point-source) scale. These components are added back as Gaussians of the size fitted to the synthesized beams and scaled by them to produce an image with correct units.

[2] the amount of each component subtracted at each iteration, usually 0.1, but values close to 1.0 were said to work well

This algorithm does not work well without some steering. The user may specify a variety of multi-scale Clean control parameters in IMAGR, but only two of them have turned out to be important. The first is the resolution-dependent flux density cutoff discussed above, passed to IMAGR via the parameter FGAUSS. In general, lower resolution images should have higher flux density cutoffs measured in Jy per the beam area of that resolution. The second important steering parameter controls the order in which facets are Cleaned. When choosing which facet to Clean, IMAGR selects the one with the largest weighted peak flux density $F_w$:

$$F_w = \frac{F}{R^b} \ , \tag{A1}$$

where $F$ is the peak flux density of the facet, $R$ is the ratio of the area of the Clean beam for the facet being Cleaned to the area of the smallest Clean beam, and $b$ is a user-specified "bias" parameter that is passed to IMAGR via the parameter IMAGRPRM(11). The general idea is to force IMAGR to select different scales with equal probability in the next major cycle. Thus, if the sky distribution is entirely composed of point sources, $F$ will be the same at all scales and the user should set $b = 0$. In the other extreme, if the sky distribution is very large and fills the image, then $F$ in Jy/beam will be proportional to the beam area of the facet being Cleaned, and the user should set $b = 1$. In practice we find that $0.2 < b < 0.7$ is appropriate for data obtained at the VLA, the precise value depending on the structure of the sky brightness distribution.

Multi-scale Clean tends to be faster than point-source Clean despite the added number of facets. The lower resolution facets Clean out a large portion of the total flux density with a modest number of components, leaving the high-resolution Clean to image point sources and the edges of objects left behind by the circular Gaussian models. Because it makes better use of the short-spacing data, multi-scale Clean also tends to reduce the negative "bowls" surrounding sources observed with missing short-spacing visibility data (e.g., Cornwell, Braun & Briggs 1999). This is illustrated in the specific case of NGC 6503 below.

### A.4. Example: NGC 6503

The images of NGC 6503 presented in this paper were produced with IMAGR's multi-scale Clean algorithm (see Section 2). Below, we use these data to illustrate the advantages of the multi-scale Clean over the default point-source Clean.

The continuum in the vicinity of NGC 6503 was imaged and deconvolved with a multi-scale Clean over an area 2.5° in diameter divided into 55 facets, using Gaussian source models of FWHM $0''$(point source), $36''$ and $108''$, flux density cutoffs of 0.21, 0.42 and 1.7 mJy/beam respectively and $b = 0.62$. The difference between the image in Fig. 1 and that obtained with a point-source only Clean for this dataset is shown in the left-hand side of Fig. 16. The boxes used in the two Cleans were identical. Because the continuum in NGC 6503 is extended (Fig. 2), the multi-scale Clean managed that area of the image rather better than the point-source Clean, and the difference between the two images at this location peaks at $\sim 60\,\mu$Jy. The rest of the continuum image is dominated by emission from unresolved objects (Fig. 1): for this distribution, the benefits of a multi-scale Clean over a point-source Clean are minimal. Nonetheless, the difference image in Fig. 16 shows a circular pattern surrounding NGC 6503, with peaks in excess of $\sim 20\,\mu$Jy. This circular pattern is the Fourier transform of the roughly circular hole in the data sampling due to missing spacings less than the antenna diameter. Multi-scale Clean appears to have removed a systematic defect from the image, reduced the noise by a few percent, and raised the flux density on the extended source by $\sim 9\%$.

The HI in NGC 6503 was imaged in each channel in a single facet, and deconvolved using a multi-scale Clean with $0''$, $36''$, $108''$ and $324''$ FHWM source models, flux density cutoffs of 0.2, 0.55, 2.6, and 7.8 mJy/beam respectively and $b = 0.62$. Because the channels in Fig. 3 contain extended emission, a multi-scale Clean performs substantially better than a point-source Clean for this cube. As an example, multi-scale Clean found 16% more flux density in 6% *more* iterations than the point-source Clean at $V = 98.3\,\mathrm{km\ s^{-1}}$ using identical boxes; see the right-hand side of Fig. 16. Relative to a point-source Clean, the multi-scale Clean of the HI data cube has eliminated most of the frequency-dependent "bowl" of negative emission indicative of missing short spacings in the visibility data. This is illustrated by the primary beam-corrected integrated spectra of NGC 6503 in Fig. 17. The dashed line in the left panel shows the flux density of NGC 6503 Cleaned and measured in a rectangular region encompassing the zeroth moment image (Fig. 8). It falls systematically below the spectrum measured from the blanked data cube discussed in Section 3.2 (solid line, reproduced from Fig. 10) because negative emission from a bowl has been included in the sum. By contrast, the dotted line shows the same flux density measurement as the solid one, but for a point-source Clean data cube of the same visibility data with the same zeroth-moment, channel-independent box area. The dotted line falls well below the dashed one because the bowl is much more pronounced in the point-source Cleaned data cube than in the multi-scale Cleaned one: 33% less flux density is measured from the former in this region. In the right-hand panel of Fig. 17, the same three integrals are plotted, but all three are restricted to the un-blanked regions of the cube that was carefully boxed during, and carefully blanked after, Cleaning. The loss of flux density due to the negative bowl has been eliminated for the multi-scale Clean (total raised from 185 to 200 Jy km $s^{-1}$), but a loss of $\sim 10\%$ remains for the point-source Clean (total raised from 124 to 182 Jy km $s^{-1}$). The cube which was Cleaned using a single large box area encompassing the full HI galaxy, but which was carefully blanked thereafter (solid line) has 3 Jy km $s^{-1}$ more total flux than the carefully Cleaned cube (dashed line), perhaps partly due to Milky Way emission and partly to regions of emission overlooked in the careful Cleaning. The general conclusion of this is that careful, channel-dependent boxing during the multi-scale imaging in not required, although some restriction of the Clean area is always recommended. Careful blanking of the resulting image cube will then eliminate noise regions and some remaining negative bowl. Note that, if there is any negative bowl, then the resulting total fluxes will be reduced by the fact that signal regions are sitting inside the bowl and so have too low a value. Since the negative bowl problem is very much worse with the point-source Clean, the reduction of the brightness within signal regions remains significant.

The disparity between the left- and right-hand sides of Fig. 17 serves as a reminder that a multi-scale Clean — as with any other deconvolution algorithm – does not preclude the need for a careful analysis of the data. Nonetheless, IMAGR's multi-scale Clean algorithm outperforms a point-source Clean for extended sources like NGC 6503, yielding a truer representation of the sky brightness distribution.

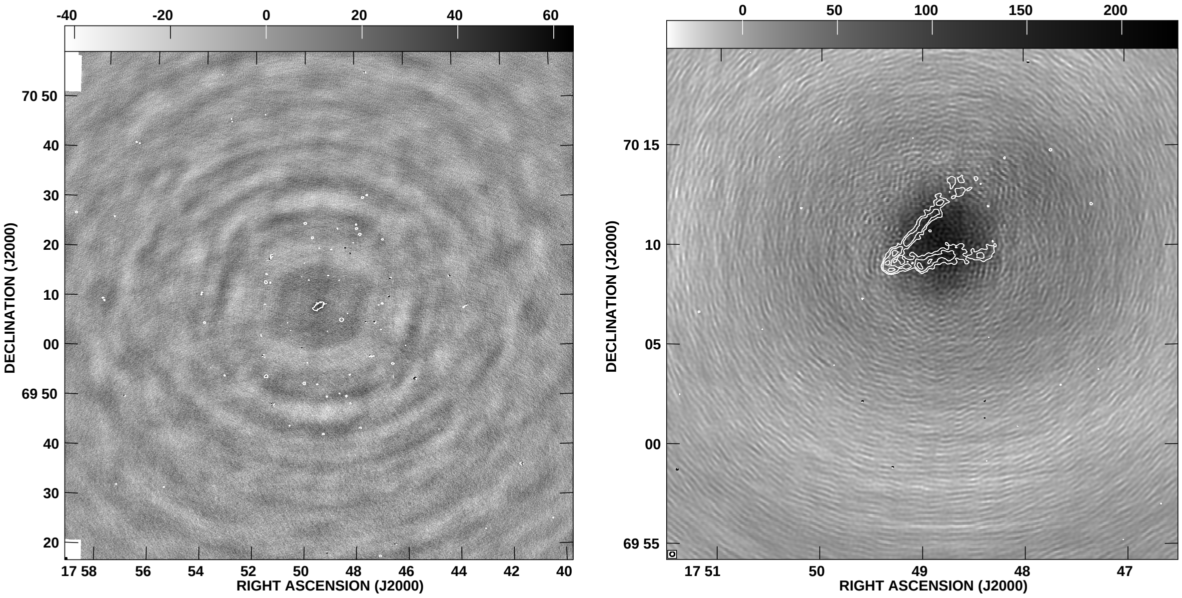


Fig. 16.— In gray-scale, the multi-scale Clean image minus point-source Clean image of (left) the continuum emission and (right) the HI line emission at $V = 98.3\,\mathrm{km\,s^{-1}}$ in NGC 6503. The gray-scale ranges are shown in the step wedges, labeled in $\mu$Jy. The multi-scale images in the continuum and the HI are sketched in with contours. The Clean beam is illustrated at the lower left corner in both images and is nearly invisible on these scales.

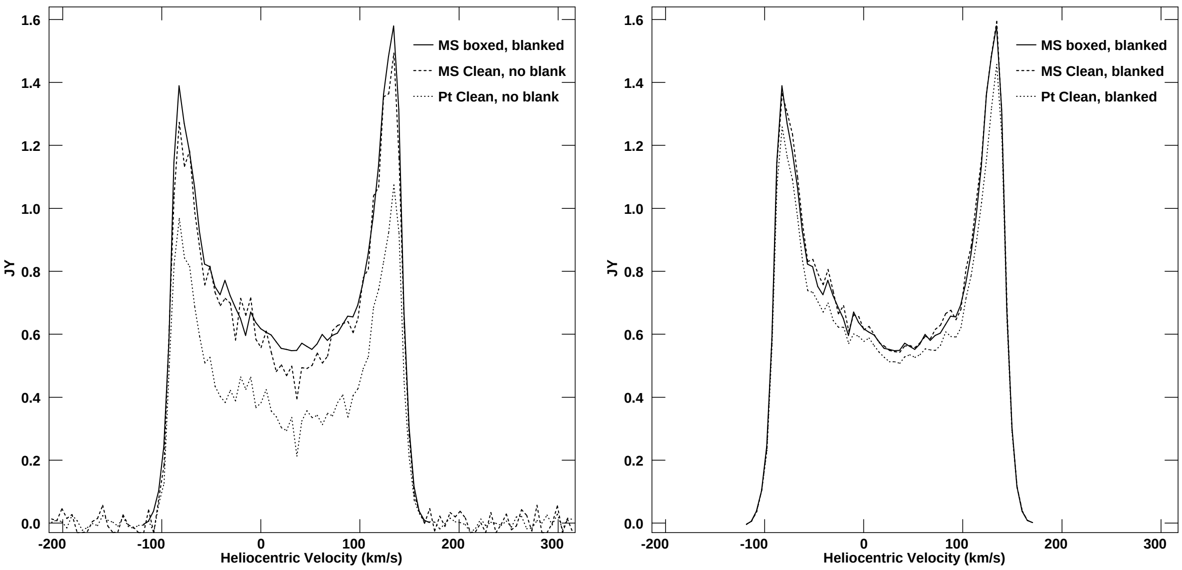


Fig. 17.— Primary beam-corrected integrated spectrum of NGC 6503 obtained using a number of Cleaning and blanking prescriptions. Left: the solid line is the integral over the blanked cube, made from a carefully boxed Clean of each channel image (reproduced from Fig. 10). The dashed line is the integrated spectrum over a rectangular region slightly larger than the extent of the zeroth moment image constructed with multi-scale Clean with little restriction of the Cleaning area. The dotted line is the integrated spectrum constructed in the same way but using only point-source Clean components. Right: Same as left, but only un-blanked regions in the carefully boxed cube are included in each profile.

## REFERENCES


Arp, H., Sulentic, J. W., Willis, A. G., & de Ruiter, H. R. 1976, ApJ, 207, L13

Barbieri, C. V., Fraternali, F., Oosterloo, T., Bertin, G., Boomsma, R., & Sancisi, R. 2005, A&A, 439, 947

Barnabè, M., Ciotti, L., Fraternali, F., & Sancisi, R. 2006, A&A, 446, 61

Boomsma, R., Oosterloo, T. A., Fraternali, F., van der Hulst, J. M., Sancisi, R. 2008, A&A, 490, 555

Boomsma, R., Oosterloo, T. A., Fraternali, F., van der Hulst, J. M., & Sancisi, R. 2005, A&A, 431, 65

Briggs, D. S., Schwab, F. R., & Sramek, R. A. 1999, in *Synthesis Imaging in Radio Astronomy II*, eds. G. B. Taylor, C. L. Carilli, & R. A. Perley, PASP, 180, 127

Broeils, A. H. & Rhee, M.H. 1997, A&A, 324, 887

Chaves, T. A., & Irwin, J. A. 2001, ApJ, 557, 646

Clark, B. G. 1980, A&A, 89, 377

Clarke, T. E., & Ensslin, T. A. 2006, AJ, 131, 2900

Collins, J. A., Benjamin, R. A., & Rand, R. J. 2002, ApJ, 578, 98

Condon, J. J., Cotton, W. D., Greisen, E. W., Yin, Q. F., Perley, R. A., Taylor, G. B. & Broderick, J. J. 1998, AJ, 115, 1693

Cornwell, T. J. 1983, å, 121, 281

Cornwell, T. J. 2008, astro-ph, arXiv:0806.2228v1, submitted to IEEE Special Issue on Signal Processing

Cornwell, T. J., Braun, R., & Briggs, D. S. 1999, in *Synthesis Imaging in Radio Astronomy II*, eds. G. B. Taylor, C. L. Carilli, & R. A. Perley, PASP, 180, 151

Cornwell, T. J. & Perley, R. A. 1992, A&A, 261, 353

Cornwell, T. J., Uson, J. M., & Haddad, N. 1992, A&A, 258, 583

de Vaucouleurs, G., de Vaucouleurs, A., Corwin, H. G., Buta, R. J., Paturel, G., & Fouqué, P. 1991, Third Reference Catalog of Bright Galaxies, Springer-Verlag, New York

Deul, E. R. & den Hartog, R. H. 1990, A&A, 229, 362

Fraternali, F., van Moorsel, G., Sancisi, R., & Oosterloo, T. 2002, AJ, 123, 3124

Fraternali, F., & Binney, J. J. 2006, MNRAS, 366, 449

Fraternali, F. & Binney, J. J. 2008, MNRAS., 386, 935

Fraternali, F. 2008, arXiv:0807.3365

Gentile, G., Salucci, P., Klein, U., & Ganato, G. L. 2007, MNRAS, 375, 199

Greisen, E. W. 2003, in Information Handling in Astronomy — Historical Vistas, (ed. A. Heck), Kluwer, Dordrecht, 109

Ho, L. C., Filippenko, A. V., Sargent, W. L. W. 1997, ApJS, 112, 315

Högbom, J. 1974, ApJS, 15, 417

Holdaway, M. & Cornwell, T. J. 1999, unpublished Mosaicing Workshop, NRAO Socorro, NM

Irwin, J. A. 1994, ApJ, 429, 618

Karachentsev, I. D. & Sharina,, M. E. 1997, A&A, 324, 457

Karachentsev, I. D., et al. 2003, A&A, 398, 479

Kaufmann, T., Mayer, L., Wadsley, J., Stadel, J., & Moore, B. 2006, MNRAS, 370, 1612

Kennicutt, R. C. 1989, ApJ344, 685

Kennicutt, R. C., Jr. 1998, ApJ, 498, 541

Kent, B. R., Spekkens, K., Giovanelli, R., Haynes, M. P., Momjian, E., Cortes, J. R., Hardy, E., & West, A. A. 2008, ApJ, in press (arXiv:0810.3571)

Kewley, L. J., Geller, M. J., Jansen, R. A., & Dopita, M. A. 2002, AJ, 124, 3135

Lira, P., Johnson, R. A., Lawrence, A. & Fernandes, R. Cid 2007, MNRAS, 382, 1552

Makarova, L. 1999, A&AS, 139, 491

Matthews, L. D. & Wood, K. 2003, ApJ, 593, 721

Miller, E. D., Bregman, J. N., & Wakker, B. P. 2008, ApJ, in press (arXiv:0810.5130)

Momjian, E., Romney, J. D., Carilli, C. L., & Troland, T. H., 2006, ApJ, 653, 1172

Oosterloo, T., Fraternali, F., & Sancisi, R 2007, AJ, 134, 1019

Rich, J. W., de Blok, W. J. G., Cornwell, T. J., Brinks, E., Walter, F., Bagetakos, I, Kennicutt, R. C. 2008, AJ, 136, 2897

Roberts, M. S. & Haynes, M. P. 1994, ARA&A, 32, 115

Sancisi, R., Fraternali, F., Oosterloo, T., & van der Hulst, T, 2008, A&A Rev., 15, 189

Schaap, W. E., Sancisi, R., & Swaters, R. A. 2000, A&A, 356, L49

Schwab, F. R. 1980, Proc. S.P.I.E., 231, 18

Schwab, F. R. 1984, AJ, 89, 1076

Shostak, G. S., Willis, A. G., & Crane, P.C. 1981, A&A, 96, 393

Silk, J. & Sunyaev, R. A. 1976, Nature, 260, 508

Sanders, D. B., Mazzarella, J. M., Kim, D.-C., Surace, J. A., & Soifer, B. T. 2003, AJ, 126, 1607

Thilker, D. A., Braun, R., & Walterbros, R. A. M. 2002, in Seeing Through the Dust: The Detection of HI and the Exploration of the ISM in Galaxies, (ed. A. R. Taylor, T. L. Landecker, & A. G. Willis), ASP, San Francisco, 276, 370

van der Hulst, J. M., Terlouw, J. P., Begeman, K. G., Zwitser, W., & Roelfsema, P. R. 1992, in Astronomical Data Analysis Software and Systems I, ASP Conf. Ser. 25, ed. D, M. Worrall, C. Biemesderfer, & J. Barnes (San Fancisco: ASP), 131

van der Hulst, J. M., Skillman, E. D., Smith, T. R., Bothen, G. D., McGaugh, S. S., & de Blok, W. J. G. 1993 , AJ, 106, 548

van Moorsel, G. A. & Wells, D. C. 1985, ApJ, 90, 1038

Verdes-Montenegro, L., Sulentic, J., Lisenfeld, U., Leon, S., Espada, D., Garcia, E., Sabater, J., & Verley, S. 2005, A&A, 436, 443

Wakker, B. P. & Schwarz, U. J. 1988, A&A, 200, 312

This 2-column preprint was prepared with the AAS LaTeX macros v5.2.